

1     **Temporal variations of the hygroscopicity and mixing state of black**  
2                     **carbon aerosols in a polluted megacity area**

3     Kangning Li<sup>1</sup>, Xingnan Ye<sup>1</sup>, Hongwei Pang<sup>1</sup>, Xiaohui Lu<sup>1</sup>, Hong Chen<sup>1</sup>, Xiaofei  
4     Wang<sup>1,2\*</sup>, Xin Yang<sup>1,2\*</sup>, Jianmin Chen<sup>1</sup>, Yingjun Chen<sup>2,3</sup>

5     <sup>1</sup>*Shanghai Key Laboratory of Atmospheric Particle Pollution and Prevention, Department of*  
6     *Environmental Science and Engineering, Fudan University, Shanghai 200433, China*

7     <sup>2</sup>*Shanghai Institute of Pollution Control and Ecological Security, Shanghai 200092, China*

8     <sup>3</sup>*College of Environmental Science and Engineering, Tongji University, Shanghai 200092,*  
9     *China*

10    Correspondence to: Xiaofei Wang (xiaofeiwang1986@gmail.com); Xin Yang  
11    (yangxin@fudan.edu.cn)

12

13    **Keywords:** aerosol, black carbon, hygroscopicity, mixing state, SP2

14

15    **Abstract.**

16    Black carbon (BC) aerosols in the atmosphere strongly affect radiative forcing. They  
17    are mainly removed from the air by wet deposition, and their lifetime is controlled by  
18    their water uptake ability or hygroscopicity, which is a function of the aerosol mixing  
19    states. It is well known that the atmospheric aging processes coat various materials on  
20    BC aerosols and affect their mixing states and hygroscopicity. However, detailed  
21    relations between the aging processes as well as the hygroscopicity and mixing state  
22    of BC aerosol particles in polluted city areas are not well understood. Here, we  
23    studied the temporal variation of the hygroscopicity and its correlation with the  
24    mixing state of ambient BC particles during 2017's summer in Shanghai, China using  
25    a hygroscopicity tandem differential mobility analyzer in-line with a single particle  
26    soot photometer (HTDMA-SP2 system) as well as a single particle aerosol mass  
27    spectrometer (SPAMS). BC particles with 120 nm, 240 nm and 360 nm dry diameter

28 were humidified at  $RH = 85\%$ . After humidification, particles with growth factors  
29 (GFs) of 1.0, 1.2, and 1.4, representing the BC particles with different  
30 hygroscopicities (hydrophobic, transition, and hydrophilic modes, respectively), were  
31 analyzed by a SP2 to obtain their BC mixing states. The diurnal trends of coating  
32 thickness and chemical mixing state show that coating materials of BC particles were  
33 distinct between daytime and nighttime. The differences were associated with the  
34 hygroscopicity of BC particles. Single particle mass spectrometry and other chemical  
35 characterization techniques revealed that with lower temperature and higher relative  
36 humidity (RH) during nighttime, formation or condensation of nitrates resulted in an  
37 enhanced hygroscopicity of BC particles. During daytime, secondary organic carbon  
38 formation was mainly responsible for the change of hygroscopicity of BC particles.  
39 Due to the high hygroscopicity of inorganic nitrate, a thinner nitrate coating on BC  
40 particles could convert fresh BC particles to aged hygroscopic ones during nighttime  
41 while a thicker coating layer of secondary materials was required to reach the same  
42 overall hygroscopicity during daytime since the participation of secondary organic  
43 carbon. Different atmospheric aging processes between daytime and nighttime led to  
44 the change of BC particles' mixing states, which play a fundamental role in  
45 determining their hygroscopicity. To our knowledge, this is the first report of links  
46 between temporal variations of the hygroscopic growth of BC particles and  
47 atmospheric aging processes in polluted environment. These findings have significant  
48 ramification in understanding the aging process, wet removal as well as climate  
49 effects of BC particles.

## 50 **1 Introduction**

51 Black carbon (BC) aerosols are a strong light absorbing component in the  
52 atmosphere and a major contributor to the positive radiative forcing (Bond et al., 2013)  
53 (Change, 2015; Kondo, 2015). They are mainly generated from incomplete  
54 combustion of fossil fuels and biomass. Fresh BC emission from traffic is  
55 hydrophobic (Lammel et al., 1995; Dusek et al., 2006). However, the particles' can be  
56 enhanced by internally mixing with secondary materials through atmospheric aging  
57 processes (Schneider et al., 2005; Shiraiwa et al., 2007; Matsui et al., 2013; Pratt et al.,  
58 2011). Hygroscopicity of BC aerosol significantly affects their removal rate through  
59 wet deposition, absorption in human's respiratory tract (Löndahl et al., 2007), optical  
60 properties (Chen et al., 2012), and their surface reactivity (Mogili et al., 2006).  
61 Therefore, it is critical to understand the relations between the atmospheric aging  
62 processes and the hygroscopicity of BC aerosols. **Atmospheric aerosols, including BC**  
63 **particles, always have various sizes with distinct chemical compositions. To better**  
64 **understand or describe an aerosol population, "mixing state" is often used. The**  
65 **definition of mixing state, provided by Winkler (1973), refers to both internal and**  
66 **external mixtures in aerosols. In an external mixture, individual particles in a given**  
67 **size range consist of different chemical species. Chemical composition of particulate**  
68 **mass in that size range will be determined by the relative contributions of the**  
69 **chemically distinct particles. In an internal mixture, on the other hand, all particles in**  
70 **a given size range are composed of the same mixture of two or more chemical**  
71 **compounds (Heintzenberg et al., 1990). The mixing state of atmospheric BC particles**  
72 **is closely linked to their sources and aging processes (Weingartner et al., 1997; Gysel**  
73 **et al., 2003; Petzold et al., 2005; Chirico et al., 2010; Heringa et al., 2011). Aerosol**  
74 **hygroscopicity is determined by the chemical composition of each individual particle**  
75 **(Heintzenberg et al., 1990; Gysel et al., 2003; McMeeking et al., 2011; Liu et al.,**  
76 **2013). Thus, aerosol mixing states play a critical role in determining the**  
77 **hygroscopicity of BC particles.**

78 Many studies have reported the mixing state of atmospheric BC particles. For  
79 example, aerosol's mixing state can be determined using a HTDMA (Swietlicki et al.  
80 2008), or a combined volatility-hygroscopicity TDMA (VHTDMA) (e.g., Johnson,  
81 2005). Shiraiwa et al., (2007) investigated the evolution of mixing state of BC using a  
82 SP2 in the polluted air transported from Tokyo city area in summer. The fraction of  
83 thickly coated BC with a core diameter ( $D_C$ ) of 180 nm increased at a rate of  $1.9\% \text{ h}^{-1}$ .  
84 The increase rates were lower for larger  $D_C$  (Shiraiwa et al., 2007). Healy et al. (2012)  
85 used an aerosol time of flight mass spectrometer (ATOFMS) to study the mixing state  
86 of BC particles in Paris. The smaller BC particles ( $D_{va} \leq 400 \text{ nm}$ ) were mainly  
87 externally mixed, indicating they were from local or regional sources, while bigger  
88 BC particles ( $D_{va} \geq 400 \text{ nm}$ ) were mainly internally mixed with nitrate, indicating  
89 they were from medium to long-range transport. Kuwata and Kondo (2008) conducted  
90 volatility TDMA (VTDMA) measurements and showed that the aerosol was often an  
91 external mixture of less- and more-volatile particles.

92 According to our knowledge, there are only a few direct measurements of BC  
93 particles' hygroscopic properties in the atmosphere. One of the previously used  
94 techniques was coupling hygroscopic measurements with VTDMA system. It was  
95 found that the less volatile aerosol components were mainly composed of BC at close  
96 proximity to urban environments (Kuwata et al., 2007; Rose et al., 2011). The  
97 relationship between hygroscopicity and mixing state of BC aerosols had been studied.  
98 BC particles exposed to subsaturated sulfuric acid vapor exhibit a large change in  
99 morphology. These particles are very hygroscopic and act as efficient  
100 cloud-condensation nuclei. Coating with sulfuric acid and subsequent hygroscopic  
101 growth increase their light scattering coefficient by 10-fold and light absorption  
102 coefficient by nearly 2-fold at  $\text{RH} = 80\%$  compared to uncoated BC particles (Zhang  
103 et al., 2008). Herich et al. (2008) combined an ATOFMS with a HTDMA to  
104 investigate the mixing state and hygroscopicity of BC-containing particles at an urban  
105 site in Zurich, Switzerland. The result shows that most of BC-containing particles

106 internally mixed with organics and combustion species ( $^{26}\text{CN}^-$  and  $^{42}\text{CNO}^-$ ). They  
107 have lower hygroscopicity compared with sulfate and nitrate mixed (Herich et al.,  
108 2008). With a similar setup, our previous study finds that condensation of amine and  
109 secondary inorganic species would enhance the hygroscopicity of submicron particles,  
110 including BC particles (Wang et al., 2014). Laborde et al., connected a SP2 in  
111 downstream of HTDMA (RH = 90%) and shows that the majority of urban aerosol  
112 particles with high hygroscopicity (GF  $\approx$  1.6) do not contain a detectable refractory  
113 BC core, while hydrophobic or less hygroscopic particles ( $1.1 \leq \text{GF} \leq 1.2$ ) have a BC  
114 core with no or little coating of soluble species (Laborde et al., 2013). Similarly, by  
115 coupling a SP2 with a HTDMA, McMeeking et al. (2011) introduced a method for  
116 measuring the hygroscopicity of externally and internally mixed BC particles. They  
117 tested this technique using uncoated and coated laboratory generated model BC  
118 compounds. The obtained information is compared to the hygroscopicity distribution  
119 of ambient BC aerosols. Their results suggest that the dominant fraction of the BC  
120 particles does not readily act as cloud condensation nuclei (CCN) at 0.2% super  
121 saturation in an urban area. In addition, Liu et al. (2013) deployed a similar  
122 instrument setup and investigated the relation between the hygroscopic properties and  
123 mixing state of BC particles (Liu et al., 2013). It shows that the GF of BC particles  
124 was influenced by the composition of soluble materials.

125         These previous studies have relied on real time hygroscopicity measurements, but  
126 usually without detailed temporal information on changes of mixing state of BC  
127 particles. Time resolved information on aerosol mixing state would be very useful to  
128 identify their sources and aging processes. During summer time in heavily polluted  
129 areas, the atmospheric aging processes could be much more complex due to higher  
130 temperature, higher pollutant concentrations, and stronger sunlight radiation.  
131 However, according to our knowledge, few studies have reported time resolved  
132 analysis on the mixing state and hygroscopicity of BC particles of particular GFs  
133 during summer time. Therefore, with high time resolution single particle analysis, this

134 field study has aimed to determine the relations between BC particle hygroscopicity  
135 and real time mixing state measurement in Shanghai, a heavily polluted megacity area.  
136 It would provide more insights on the effects of atmospheric processes on  
137 hygroscopicity of BC particles.

## 138 **2 Experimental section**

### 139 **2.1 HTDMA-SP2 system**

140 Temporal variation of BC aerosols mixing state and hygroscopic property were  
141 measured using a custom-built HTDMA-SP2 system (Fig. 1). **Similar to systems that**  
142 **couple an HTDMA with another instrument, such as those used by Herich et al.**  
143 **(2008), Zelenyuk et al. (2008), and Wang et al. (2014), our system used an SP2 (DMT,**  
144 **Boulder, CO, USA) in the downstream of an HTDMA to measure rBC content as a**  
145 **function of hygroscopicity.** The first DMA in the HTDMA system selects  
146 **monodisperse dried particles.** Then the selected aerosols are humidified at a specified  
147 relative humidity (RH=85% in this study). The size distribution of humidified (wet)  
148 particles is measured by a scanning mobility particle size (SMPS), which includes  
149 another DMA and a condensation particle counter (CPC, model 3771, TSI Inc.). GF is  
150 the ratio between particle wet size and dry size. **The two DMAs were operated with**  
151 **recirculating sheath flows and a sheath-to-sample flow ratio of 10:1.** The HTDMA is  
152 **encapsulated in a thermostatted box to reduce temperature fluctuations.** The DMA  
153 **housing temperature was controlled at 20°C.** Aerosol flow was set at 0.43 L/min (the  
154 **sum of the CPC (0.4 L/min) and the SP2 (0.03 L/min) flow rates).** The hygroscopicity  
155 **measurement was calibrated using (NH<sub>4</sub>)<sub>2</sub>SO<sub>4</sub> particles.** The SP2 identifies  
156 BC-containing particles at each selected GF. The water uptake properties of BC  
157 particles can be linked directly to the mixing state measured by SP2.

158 **SP2 can measure number and mass size distribution of rBC containing particles**  
159 **(Baumgardner et al., 2004; Schwarz et al., 2006).** Briefly, SP2 detects incandescence

160 and scattering light signals of rBC-containing particles induced by a 1064 nm Nd:  
161 YAG intra-cavity laser. The mass of rBC is proportional to the intensity of the  
162 incandescence signal. A particle with an incandescence signal (above a threshold) is  
163 treated as an rBC particle, while a particle that only exhibits scattering signal is  
164 considered as a non-rBC particle. SP2 detection efficiency was close to unity for  
165 larger rBC particles. The minimum rBC mass that could be observed with near-unity  
166 detection efficiency was  $\sim 0.7$  fg rBC, corresponding to 90 nm mass equivalent  
167 diameter; the detection efficiency declined rapidly at lower sizes (Gong et al.; 2016).  
168 The total ambient mass concentrations of rBC were possibly underestimated because  
169 of the reduced detection efficiency for small rBC particles (Schwarz et al., 2006;  
170 McMeeking et al., 2010).

171 The conversion from rBC mass to the effective rBC core diameter requires to  
172 assume an effective density for rBC cores in the particles. In this study, an effective  
173 density of  $1.8 \text{ g cm}^{-3}$  was used to convert the ambient rBC mass to the mass  
174 equivalent diameter. This value was recommended by many previous studies (Bond  
175 and Bergstrom, 2006; Gong et al., 2016).

176 The scattering properties of externally and internally mixed rBC particles may be  
177 distorted due to particle mass loss induced by laser heating in SP2. Thus, scattered  
178 light from an rBC particle may not yield a full Gaussian waveform. The Gaussian  
179 scattering function was reconstructed from the leading edge of the scattering signal  
180 (before particle is heated by the laser), which was measured with a two-element  
181 avalanche photodiode (APD). This method can determine the scattering properties of  
182 individual rBC particles more accurately (so called LEO-fit method; Gao et al., 2007).  
183 Optical diameter of an rBC particle ( $D_p$ ) was derived from Mie theory with the LEO  
184 fitted scattering signal and rBC core size ( $D_c$ ) (Moteki et al., 2010; Liu et al., 2014;  
185 Laborde et al., 2013). The absolute coating thickness of an rBC particle was  
186 calculated as  $(D_p - D_c)/2$ , based on the assumption of a concentric core-shell  
187 morphology. However, rBC aging in the atmosphere may result in an imperfect

188 core-shell structure (Matsui et al., 2013).

189 In this study, ambient particles with three electrical mobility sizes (120 nm, 240  
190 nm and 360 nm in dry diameter) were selected by first DMA, then humidified at a  
191 RH=85%. For the measurement of the overall hygroscopic distribution of total  
192 ambient particles (such as Fig. 3(a)), the second DMA was operated in a scanning  
193 continuous mode. For the measurement of temporal trends of the hygroscopic  
194 distribution, the second DMA was operated in a stepped mode by sending particles  
195 with fixed GFs of 1.0, 1.2 and 1.4 (representing hydrophobic, transition and  
196 hydrophilic mode, respectively) to the CPC and SP2.

## 197 **2.2 Single particle aerosol mass spectrometer (SPAMS)**

198 A single particle aerosol mass spectrometer (SPAMS Hexin Analytical  
199 Instrument Co., Ltd., China) was used in parallel to the HTDMA-SP2 system. The  
200 SPAMS first measures the size of a single aerosol particle. Then, it uses a 266 nm  
201 laser to disintegrate the particle and ionize its chemical compounds, of which  
202 mass-to-charge ratios ( $m/z$ ) and concentration are determined by a bipolar  
203 time-of-flight mass spectrometer. Detailed information on the SPAMS has been  
204 described elsewhere (Li et al., 2011).

205 In this work, a total of 158,410 individual particle mass spectra were collected,  
206 accounting for about 56% of all the particles that were sized in the SPAMS. Element  
207 carbon ion clusters has been considered an important marker for BC aerosols (Gong et  
208 al., 2016). Using  $C_n^{+/-}$  ( $n=1, 2, 3\dots$ ) as the BC marker, a total of 64,368 BC-containing  
209 particles were identified, accounting for about 40.1% of sampled particles. The mass  
210 spectra of BC-containing particles were classified into several types based on their  
211 similarities using a clustering algorithm called adaptive resonance theory (ART-2a)  
212 (Song et al., 1999). Similar to previous studies (Huang et al., 2013; Zhai et al., 2017)  
213 (Gong et al., 2016; Spencer et al., 2007), the vigilance factor, learning rate, and

214 iterations for ART-2a algorithm were set to 0.85, 0.05, and 20, respectively. Finally,  
215 five particle types were manually combined based on the similarity of their chemical  
216 nature.

217 Noticeably, the particles with mobility size at 120 nm cannot be detected by the  
218 SPAMS, as they were smaller than the lower limit (200 nm) of size range of the  
219 SPAMS. According to Slowik's study, the vacuum aerodynamic diameter ( $d_{va}$ ) of  
220 compact aggregated BC particles was linearly proportional to mobility diameter ( $d_m$ ),  
221 specifically,  $d_{va} = 1.3*d_m$  (Slowik et al., 2004). Here we assume that most detected BC  
222 particles follows this relation ( $d_{va} = 1.3*d_m$ ). In this study, only particles with  $D_0 =$   
223 120 nm, 240 nm, and 360 nm were studied with the HTDMA-SP2 system. These  
224 mobility sizes correspond to  $d_{va} = 150$  nm, 312 nm and 468 nm, respectively. Thus,  
225 the SPAMS cannot provide mixing state information for particles with  $d_{va} = 150$  nm  
226 ( $d_m = 120$  nm), which was out of the SPAMS detection range (200 to 2000 nm).

## 227 **2.3 Other instruments**

### 228 **2.3.1 OC/EC analyzer**

229 Hourly mass concentrations of elemental carbon (EC) and organic carbon (OC)  
230 were measured by a semi-continuous OC/EC analyzer (Model 4, Sunset Laboratory  
231 Inc., Portland, USA.) based on the National Institute of Occupational Safety and  
232 Health thermal/optical transmittance measurement protocol (NIOSH 5040), with a  
233  $PM_{2.5}$  impactor inlet. Detailed information can be found in the previous publication  
234 (Wang et al., 2016a). Concentration of secondary organic carbon (SOC) was  
235 estimated using the method of minimum ratio of OC/EC (Chou et al., 2010), which is  
236 calculated by the following equation.

$$237 \quad SOC = OC_{total} - EC \times (OC/EC)_{pri} \quad (1)$$

238 Where OC and EC are the measured hourly mass concentrations of organic

239 carbon and elemental carbon.  $(OC/EC)_{pri}$  is the OC/EC ratio **in primarily emitted**  
240 **combustion aerosols**. At urban locations, the  $(OC/EC)_{pri}$  was assumed to be the  
241 minimum value of OC/EC ratio throughout the whole study sampling period (Cao et  
242 al., 2013). The OC vs EC plot is displayed in Fig. S1. We use the minimum value 2.2  
243 as the  $(OC/EC)_{pri}$ , in this work.

### 244 **2.3.2 Monitor for Aerosols and Gases in Air (MARGA)**

245 A Monitor for Aerosols and Gases in Air (MARGA, Applikon Analytical B. B.  
246 Corp., ADI 2080, Netherlands), with a  $PM_{2.5}$  cyclone impactor, was deployed to  
247 measure the concentrations of inorganic ionic species (i.e.  $SO_4^{2-}$ ,  $NO_3^-$  and  $NH_4^+$ ) in  
248  $PM_{2.5}$ . Detailed description about the MARGA is available in the previous publication  
249 (Du et al., 2010).

### 250 **2.4 Sampling period and site**

251 The measurements of the relationship between mixing state and hygroscopicity  
252 of BC particles various with time were carried out from 4 to 16 July 2017 using a  
253 SPAMS and a HTDMA-SP2 system. The sampling site is located at the Department  
254 of Environmental Science and Engineering on the main campus of Fudan University  
255 (31.30°N, 121.5°E), and it is surrounded by residential and commercial areas. An  
256 elevated road (the Middle Ring Line) with heavy traffic is ~ 400 m away from the  
257 sampling location.

### 258 **2.5 Meteorology**

259 The meteorology and air quality information were obtained at a nearby air  
260 quality monitoring station, which is operated by Shanghai Environmental Monitoring  
261 Center (Yangpu Site). (<http://www.semc.com.cn/aqi/home/Index.aspx>). The station  
262 was 3.3 km from the sampling site. Temporal profiles of measured gaseous pollutants  
263 ( $O_3$ ,  $SO_2$ , CO, and  $NO_2$ ), temperature, relative humidity (RH),  $PM_{2.5}$ , and hourly  $PM_{10}$

264 mass concentrations from July 4 to 16, 2017 are shown in Fig. 2. The temperature and  
265 RH varied between 24.1°C and 38.0 °C, and 46% and 100%, with an average of 30.4  
266 °C, 74.1%, respectively, during the sampling period. Fig. 2 shows that the temperature  
267 was negatively correlated with RH, but positively correlated with O<sub>3</sub> mass  
268 concentration. Hourly O<sub>3</sub> concentration usually peaked in the afternoon during this  
269 period. Its maximum value reached 316 µg/m<sup>3</sup> at 14:00 on July 12, showing  
270 extremely active photochemical activities in this afternoon. The maximum value of  
271 PM<sub>2.5</sub> reached 72 µg/m<sup>3</sup> at 18:00 on July 13, with an average of 29.2 µg/m<sup>3</sup>.  
272 Meanwhile, PM<sub>10</sub> varied from 15 to 141 µg/m<sup>3</sup>, with an average of 57.9 µg/m<sup>3</sup>.

### 273 **3 Results and discussion**

274 The focus of this paper is temporal variation of hygroscopicity and mixing states  
275 of ambient BC particles. Due to the slow scanning rate of DMA voltage and sampling  
276 time requirement of SP2, obtaining temporal information of BC concentrations  
277 requires the DMA size selection to be fixed for a certain amount of time. Therefore,  
278 for HTDMA-SP2 system, only one size (D<sub>0</sub>) was studied for each sampling period.  
279 Specifically, D<sub>0</sub> = 120, 240, and 360 nm was measured during 2017/07/04 06:00:00~  
280 2017/07/07 05:00:00, 2017/07/07 06:00:00~2017/07/10 05:00:00, and 2017/07/10  
281 06:00:00~2017/07/16 05:00:00, respectively.

282 We studied three GFs (GF=1.0, 1.2, and 1.4) for each D<sub>0</sub>. The GF selection was  
283 based on the GF size distribution of BC particles. A general picture of hygroscopicity  
284 of total sampled ambient particles is shown in Fig. 3(a), which illustrates averaged  
285 hygroscopic growth factor distributions at three selected sizes (D<sub>0</sub> = 120, 240, and 360  
286 nm). All three GF curves featured a bimodal distribution, which contained a  
287 hydrophobic mode peak at GF = ~1.0 and a hydrophilic mode peak at larger GFs (1.3  
288 ~ 1.6). Clearly, the hygroscopic particles were typically more abundant than the  
289 hydrophobic ones. These hygroscopic particles featured a size dependent hygroscopic  
290 growth, significantly shifting to larger GF with increasing particle size. This feature

291 was conventionally attributed to a size dependent chemical composition (Swietlicki et  
292 al., 2008; Ye et al., 2013). In contrast, hygroscopic growth factor distributions of BC  
293 particles only show one mode (Fig. 3(b)). The GF curve of BC particles peaked at GF  
294 = ~1.0. The BC-containing number fraction decreased sharply for larger GFs. When  
295 GF was greater than 1.4, few BC particles were detected by SP2.

296 GF=1.0, 1.2 and 1.4 were selected to represent hydrophobic, transition, and  
297 hydrophilic mode for BC particles, respectively. Higher GFs (GF>1.4) were not  
298 selected due to the low BC-containing number fractions at these GFs. For each day,  
299 the sampling was divided to eight 3-hour sampling periods. Three GFs (GF=1.0, 1.2  
300 and 1.4) were set sequentially for one hour during each sampling period.

301 Here, the diurnal trend (in Section 3.1) and classification (in Section 3.2) of BC  
302 particles are described and discussed in detail. Then, the relations between mixing  
303 state and hygroscopicity of BC particles are elucidated (in Section 3.3).

### 304 **3.1 Diurnal variations of BC particles with different hygroscopicities**

#### 305 **3.1.1 Diurnal variation of hydrophobic mode BC particles**

306 The averaged diurnal patterns of the number concentration and number fraction  
307 of BC particles are shown in Fig. 4(a) and 4(b), respectively. The number fraction of  
308 BC particles is defined as the ratio of the number concentration of sampled refractory  
309 BC particles to that of total samples, including refractory BC and non-BC particles, at  
310 a certain  $D_0$  and GF. The majority of hydrophobic mode (GF=1.0) BC particles  
311 typically exhibited two peaks for all three  $D_0$ s (Fig. 4(a)). They were likely to be  
312 freshly emitted from combustion sources (McMeeking et al., 2011). The number  
313 concentrations of hydrophobic BC particles reached their first peak in the morning  
314 around 6:00 to 9:00 local time (LT), and then followed by a dip in the afternoon  
315 around 12:00 to 17:00. The hydrophobic BC particles reached the second peak in the  
316 evening and then slowly decreased during the night. This trend is similar to some field

317 studies in other city areas, such as Shenzhen and Xiamen in China (Huang et al., 2012;  
318 Wang et al., 2016b). The elevated BC particle number concentration in the morning  
319 and early evening can be explained by increases in local anthropogenic emissions,  
320 especially those from rush hour traffic (Dreher et al., 1998; Allen et al., 1999;  
321 Bhugwant et al., 2000). This trend presumably was also intensified by lower boundary  
322 layer heights at those times.

323 As shown in Fig. 4(b), hydrophobic BC particles accounted for the largest  
324 percentage among three GFs for all  $D_0$ s. However, the number fractions of  
325 hydrophobic BC particles decreased with the increased  $D_0$ . For  $D_0 = 120$  nm, 240 nm,  
326 360 nm, the maximum number fractions of the hydrophobic BC particles were ~80%,  
327 70% and 60%, respectively. One possible reason is that the majority of fresh BC  
328 particles diameter are smaller than 200 nm (Kondo et al., 2006), corresponding to our  
329 finding that relatively lower fractions of BC particles were detected at larger sizes. In  
330 addition, factors affecting the BC number fractions at  $GF = 1.0$  may also be related to  
331 the behavior of non-BC containing particles and their size dependence.

### 332 3.1.2 Diurnal variations of transition and hydrophilic mode BC particles

333 The transition and hydrophilic mode BC particles likely originated from aged  
334 particles. Condensation of hydrophilic secondary materials (e.g. sulfate, nitrate and  
335 secondary organic compounds) would significantly enhance the water uptake ability  
336 of BC particles. As shown in Fig. 4(a), the number concentrations of some transition  
337 and hydrophilic mode BC particles (like transition mode for 120 and 240nm BC  
338 particles) showed a clear daily maximum during 12:00 ~ 15:00 (Fig. 4(a)). This trend  
339 could be explained by the intense aging processes during this time when sunlight  
340 intensity and atmospheric oxidants' concentration reach their peak values. However,  
341 the number concentration of transition and hydrophilic mode BC particles could be  
342 affected by other atmospheric aging processes. For example, nitrate formation could  
343 be significantly enhanced during nighttime due to the hydrolysis of  $N_2O_5$

344 (Mozurkewich et al., 1988; Wang et al., 2009; Wang et al., 2016a). This process  
345 would make more transition and hydrophilic mode BC particles during nighttime. To  
346 understand their diurnal trends, the measurement of their chemical compositions and  
347 mixing states is essential, which will be discussed in Section 3.3.

348 Fig. 4(b) also shows the diurnal variations of number fractions of transition and  
349 hydrophilic mode BC particles. Unlike the hydrophobic mode BC particles, the  
350 transition and hydrophilic mode (GF = 1.2 and 1.4) BC particles with larger sizes  
351 tended to contribute higher number fractions of total particles. This trend was more  
352 pronounced for the hydrophilic mode (GF = 1.4): the maximum number fractions of  
353 BC particles were ~10%, 10% and 20% for  $D_0 = 120$  nm, 240 nm, 360 nm,  
354 respectively. One possible reason is that the sizes of fresh BC particles are likely to be  
355 small. The median diameter of BC particles originated from traffic emissions are  
356 usually < 200 nm (Harris et al., 2001; Zervas et al., 2006; Xue et al., 2015). They have  
357 to grow to larger sizes (e.g. 360 nm) through ageing/coating, which also increases  
358 their hygroscopicity. Another possible reason is that these hydrophilic BC particles  
359 were from a different source. A candidate is biomass burning (BB) aerosols, which  
360 have slightly higher hygroscopicity than those from traffic emissions (Laborde et al.,  
361 2013). Detail discussion of BB aerosol will be shown in Section 3.2.

362 In addition, the diurnal variations of the BC particle number fraction showed that  
363 during nighttime, a larger proportion of BC particles were in hygroscopic mode  
364 compared to daytime, indicating that hygroscopicity of BC at night was much  
365 stronger than that in the daytime. The main reason will be discussed in Section 3.3.

### 366 3.1.3 Diurnal variations of rBC core diameter and coating thickness

367 rBC core diameter ( $D_c$ ) can be obtained if knowing single particle BC mass and  
368 assuming that the core is spherical and BC density is  $1.8 \text{ g/cm}^3$ . The corresponding  
369 coating thickness is  $(D_p - D_c)/2$  (Gong et al., 2016). Diurnal variations in average rBC  
370 core diameter and coating thickness at different GFs are displayed in Fig. 5(a) and Fig.

371 5(b), respectively. For a certain BC particle size, a larger core size and a thinner  
372 coating thickness corresponded to BC particles with lower hygroscopicity (e.g.  
373  $GF=1.0$ ). When BC particles became more hygroscopic (i.e.  $GF$  increases), the  
374 coating thickness increased.

375 It's interesting to note that the core sizes for the hygroscopic mode BC particles  
376 increased during nighttime (21:00 to 6:00) while coating thickness decreased (since  
377 the entire electron mobility diameter was fixed). This observation suggests that the  
378 coating material on BC particle might be different between daytime and nighttime. To  
379 achieve the same  $GF$ , an increased coating thickness is required for less hygroscopic  
380 coating materials, as the hygroscopicity of rBC core is always constant ( $GF = 1.0$ ).

381 In this study, the main uncertainty associated with the HTDMA-measured  $GF$  of  
382 soot particles was influenced by particle morphology. For fresh BC particle with an  
383 aggregate structure, the mobility diameter ( $D_{mob}$ ) measured by a DMA is normally  
384 larger than its geometric volume/mass equivalent diameter ( $D_{ve}$ ) (DeCarlo et al.,  
385 2004). However, coating on soot aggregates can modify its morphology (Weingartner  
386 et al., 1997; Lewis et al., 2009; Pagels et al., 2009) by making soot aggregate more  
387 compact. Change of particle morphology affects  $D_{mob}$  measurement. It has been  
388 reported that more compact BC particles tend to exhibit smaller mobility diameter and  
389 higher effective density (Zhang et al., 2008; Pagels et al., 2009). In HTDMA  
390 measurements, if BC-containing particles' shape are significantly fractal, the water  
391 adsorption process in HTDMA would likely make them more compact, and therefore  
392 their  $GF$ s soot particles would be underestimated. These effects are less pronounced  
393 for particles which are less fractal. Due to the limitation of HTDMA, the complex  
394 morphology or  $\rho_{BC}$  of BC-containing particles cannot be explicitly determined in this  
395 study. Thus, a conventional core-shell model for a BC-containing particle has to be  
396 assumed. The  $GF = 1.0$  results show an average coating thicknesses of  $\sim 20-35$  nm,  
397 suggesting the presence of non-BC materials or the effect of non-spherical shape on  
398 size measurement.

### 399 **3.1.4 Diurnal variations of the distribution of BC particle growth factors**

400 Fresh BC particles usually have low GF. Through ageing process, the GF of BC  
401 particles increase. It would be interesting to see how the GF distributions of BC  
402 particle change during a day and get a rough estimate of how fast the ageing process  
403 went. Fig. 6 shows the diurnal variations of the distribution of BC particle growth  
404 factors. Note only three GFs were measured by HTDMA-SP2 system. Here, the BC  
405 aerosol number fraction for each GF is defined as (BC aerosol number concentration  
406 for this GF)/(sum of BC aerosol number concentration for GF = 1.0, 1.2 and 1.4). It is  
407 found that the BC aerosol number fraction for GF = 1.0 reached two maxima at  
408 around 9:00 and 18:00, probably due to the rush hour traffic. Only 3 hours after 9:00  
409 or 18:00, the BC aerosol number fractions for GF = 1.0 dropped significantly (from  
410 0.44 to 0.26 and from 0.40 to 0.36, respectively). Meanwhile, the BC aerosol number  
411 fractions for GF = 1.4 increased (from 0.34 at 9:00 to 0.49 at 12:00 and from 0.44 at  
412 18:00 to 0.50 at 21:00). Evidently, the GF distribution of BC particles changed rapidly  
413 even in just three hours. This change was probably due to the BC particle ageing and  
414 the ageing time scale is around several hours.

415 The coating thickness of BC particles from this study (20 ~ 80 nm for BC  
416 particles with electrical mobility diameter of 120 ~ 360 nm) were in the range of  
417 previous measurements from other cities. For example, Laborde et al., measured BC  
418 coating thickness in Paris during a winter time (Laborde et al., 2013). They found  
419 coating thickness was approximately 33 nm on average for rBC core size from 180 to  
420 280 nm. Liu et al., reports an average coating thickness of ~ 40 nm for BC particles  
421 with electrical mobility diameter of 163 nm (Liu et al., 2013). A field study in London  
422 during wintertime shows that the average coating thickness for BC particles with 137  
423 nm, 143 nm and 169 nm in diameter were ~ 15 nm, 22 nm and 33 nm, respectively  
424 (Liu et al., 2014).

425 The rapid change in BC particle coating thickness suggests that the ageing time

426 scale was around several hours. This time scale is consistent with a previous modeling  
427 study (Riemer et al., 2004).

### 428 3.2 BC-containing particle types identified by SPAMS

429 The mixing state and aging degree of BC-containing particles have been studied  
430 using a SPAMS. Noticeably, the particles size range for the SPAMS is from 200 to  
431 2000 nm. The detection efficiency drops rapidly below 400 nm and above 1200 nm  
432 (Li et al., 2011). However, most pure BC particles are smaller than 200 nm (Kondo et  
433 al., 2006), which is close to the lower size limit for the SPAMS and can only be  
434 detected at a low efficiency. Based on SPAMS mass spectra patterns, BC particles  
435 were classified into five types: EC, NaKEC, ECO, KEC, and Others. Their relative  
436 contributions are shown in Table 1. The average mass spectra for each particle type  
437 are shown in Fig. S2.

438 Pure EC particles only presented BC fragment ions ( $C_n^+$  and  $C_n^-$ ) in both positive  
439 and negative ion mass spectra. There were low signals of secondary species, such as  
440 sulfate or nitrate, indicating that pure EC had not gone through significant aging in the  
441 atmosphere, thus the EC type were freshly emitted BC particles.

442 NaKEC particles exhibited strong signals for BC fragment ions in both positive  
443 and negative mass spectra, additionally, potassium ( $^{39}K^+$ ) and sodium ( $^{23}Na^+$ ) in  
444 positive ion mass spectra, as well as nitrate ( $^{46}NO_2^-$  and  $^{62}NO_3^-$ ) and sulfate ( $^{97}HSO_4^-$ )  
445 in the negative ion mass spectra also exhibited strong signals. Hydrocarbon-like  
446 organic aerosol (HOA) is dominated by alkyl fragment signatures as well as the  $C_nH$   
447  $_{2n+1}^+$  ( $m/z= 29, 43, 57$ ) and  $C_nH_{2n-1}^+$  ( $m/z= 27, 41, 55$ ) ions. The time series of HOA  
448 correlated well with those of  $NO_2$  and  $CO$ , two tracers of vehicle emissions (Fig.  
449 S3(a)). The diurnal pattern of HOA ion intensity further suggests the association of  
450 HOA with traffic activities, as it showed two obvious peaks during the morning and  
451 evening rush hours (Li et al., 2017). HOA as a tracer of traffic emission correlated  
452 reasonably well with the NaKEC particles number ( $R^2=0.560$ ), as shown in Fig.

453 S3(b).

454 The ECOC type particles internally mixed with many organic carbon (OC)  
455 signals, including  $^{+37}\text{C}_3\text{H}$ ,  $^{+43}\text{CH}_3\text{CO}^+$ ,  $^{+50}\text{C}_4\text{H}_2^+$ ,  $^{+51}\text{C}_4\text{H}^+$ ,  $^{+61}\text{CH}_3\text{C}(\text{OH})=\text{OH}^+$ ,  
456  $^{+62}(\text{CH}_3)_2\text{NHOH}^+$ , as well as  $^{+23}\text{Na}^+$  and BC fragment ions ( $\text{C}_n^+$ ). The presence of a  
457 high signal intensity for sulfate ( $^{-97}\text{HSO}_4^-$ ) and a relatively low signal intensity for  
458 nitrate ( $^{-46}\text{NO}_3^-$ ,  $^{-62}\text{NO}_3^-$ ) suggests that they were aged BC particles. BC particles with  
459 various intensities of OC, nitrate and sulfate were commonly detected in ambient  
460 measurements by ATOFMS (Moffet et al., 2008; Ault et al., 2009) (Dall'Osto and  
461 Harrison, 2006) and were also attributed to aged traffic emissions (Healy et al., 2012).

462 KEC particles were characterized by an intense  $^{+39}\text{K}^+$  signal in the positive ion  
463 mass spectra and strong signals for  $^{-26}\text{CN}^-$  and  $^{-42}\text{CNO}^-$  in the negative ion mass  
464 spectra. Significant intensities of ion fragments of levoglucosan, such as  $^{-71}\text{C}_3\text{H}_3\text{O}_2^-$   
465 and  $^{-73}\text{C}_3\text{H}_5\text{O}_2^-$ , were also observed. Typical BC fragments  $\text{C}_n^-$  appeared in the negative  
466 ion mass spectra. Similar to ECOC type, the presence of a high signal intensity of  
467  $^{-97}\text{HSO}_4^-$ ,  $^{-46}\text{NO}_2^-$  and  $^{-62}\text{NO}_3^-$  signals indicates significant particle aging in the  
468 atmosphere (Leskinen et al., 2007; Reid et al., 2005). These characteristics suggest  
469 that their sources are biomass burning or coal combustion or both (Andreae, 1983;  
470 Soto-Garcia et al., 2011; Wang et al., 2013; Gong et al., 2016). Particles with similar  
471 mass spectral patterns were previously observed in several urban field studies were  
472 also assigned to the sources of combustion of biomass or coal (Moffet et al., 2008;  
473 Healy et al., 2012; Bi et al., 2011; Wang et al., 2013; Gong et al., 2016).

474 The “Others” particle type was not grouped to any of the previous four types;  
475 and it accounts for only 8.5% in total BC particle number concentration. The average  
476 mass spectra of this particle type is displayed in Fig. S2 (e). However, this is not the  
477 focus of this study.

478 The relative fractions of aerosol types as a function of particle size were plotted

479 in Fig. S4. Generally, the number fraction for each particle type is highly dependent  
480 on particle size. Sharp changes in BC particle mixing states has been found between  
481 the size ranges of 200 nm ~ 400 nm and 400nm ~ 800nm. EC and NaKEC types are  
482 the major fraction types in the 200 nm ~ 400 nm size range. In contrast, the larger size  
483 range (400 nm ~ 800 nm) was dominated by ECOC and KEC types. For convenience  
484 of discussion, we separated particles to two groups based on their  $d_{va}$ , namely  $G_{200-400}$   
485 ( $200 \text{ nm} < d_{va} < 400 \text{ nm}$ ) and  $G_{400-800}$  ( $400 \text{ nm} < d_{va} < 800 \text{ nm}$ ). In this work,  $d_{va} = 150$   
486 nm ( $d_m = 120 \text{ nm}$ ) was out of the SPAMS detection range, while  $d_{va} = 312 \text{ nm}$  ( $d_m =$   
487  $240 \text{ nm}$ ) and  $d_{va} = 468 \text{ nm}$  ( $d_m = 360 \text{ nm}$ ) were falling in the range of  $G_{200-400}$  and  
488  $G_{400-800}$ , respectively.

489 The diurnal variations of number fraction of each particle type in  $G_{200-400}$  were  
490 calculated and shown in Fig. 7(a). It is found that number fraction of the EC and  
491 NaKEC types displayed pronounced diurnal patterns with two major peaks in the  
492 early morning (6:00 ~ 9:00) and in the evening (18:00 ~ 21:00), possibly relating to  
493 traffic. From the hygroscopicity measurement ( $D_0 = 240$  and  $360 \text{ nm}$  in Fig. 4(a)), the  
494 elevated BC particle number concentration at  $GF=1.0$  during these two time-frames  
495 suggests that the elevated concentrations of hydrophobic BC particles aerosol were  
496 probably associated with EC and NaKEC types, which are produced from traffic  
497 sources.

498 A different pattern has been observed for  $G_{400-800}$  (shown in Fig. 7(b)). The  
499 ECOC and KEC types accounted for the major number fractions in the 400 nm ~ 800  
500 nm range. The diurnal variations of these two particle types share a similar trend,  
501 while other two types (EC and NaKEC) showed no significant variation. The EC and  
502 NaKEC types only attributed to small proportions of  $G_{400-800}$  particles. Interestingly,  
503 the number fraction of ECOC in  $G_{400-800}$  also showed two major peaks in the morning  
504 and evening, suggesting that ECOC was aged BC particles from traffic emissions. The  
505 KEC peak in the evening was much more pronounced than that in the morning, and  
506 this might be due to biomass burning which is still widely used by domestic cooking

507 (in the evening) in the countryside around Shanghai city. These BB aerosols were  
508 then transported to the sampling site.

### 509 **3.3 The relations between the mixing state and hygroscopicity of BC particles**

510 To elucidate the relation between mixing state and hygroscopicity of BC  
511 particles, the detailed chemical composition and mixing state information from the  
512 EC/OC, MARGA, and SPAMS were compared to the HTDMA-SP2 hygroscopicity  
513 measurements. As discussed in Section 3.1, we found that the rBC core sizes for the  
514 hygroscopic mode particles increased during nighttime (21:00 ~ 6:00) while coating  
515 thickness decreased, indicating the BC particle coating compositions were different  
516 between daytime and nighttime. The major secondary aerosol coating materials in  
517 polluted boundary layer could be secondary organic carbon (SOC), sulfate and nitrate.  
518 Therefore, the diurnal trends of these species have been investigated and compared to  
519 BC particles' hygroscopicity.

#### 520 **3.3.1 Major secondary ionic species**

521 The dominant ionic species in urban aerosols in Shanghai are sulfate, nitrate and  
522 ammonium (Ye et al., 2013). To study the chemical composition dependence on  
523 hygroscopicity, mass concentrations of  $\text{SO}_4^{2-}$ ,  $\text{NO}_3^-$  and  $\text{NH}_4^+$  were measured by a  
524 MARGA during this field study. As shown in Fig. 8(c), the average sulfate  
525 concentration varied in a small range from ~ 4.8 to 6.1  $\mu\text{g}/\text{m}^3$ . Its concentration in the  
526 daytime was only slightly higher than that of nighttime. The average mass  
527 concentration of  $\text{NO}_3^-$  varied between 1.1  $\mu\text{g}/\text{m}^3$  and 4.4  $\mu\text{g}/\text{m}^3$  with an average of 2.3  
528  $\mu\text{g}/\text{m}^3$ . Similar to our previous study (Wang et al., 2016a), the nitrate concentrations  
529 at night were clearly elevated (Fig. 8(d)). The relative peak area (RPA) of  $\text{NO}_3^-$  in  
530 BC particles measured by SPAMS is also consistent with the MARGA measurement  
531 (Fig. 8(d)). During the nighttime in summer, lower temperature, higher relative  
532 humidity and high concentration of  $\text{NO}_3$  ( $\text{N}_2\text{O}_5$ ) favor the formation of nitrate in

533 particle phase (Wang et al., 2009; Wang et al., 2016a).

### 534 **3.3.2 Elevated SOC concentrations in the daytime**

535 Photochemical reactions are a major formation pathway of SOC (Kroll and  
536 Seinfeld, 2008; Zhang et al., 2018). Odd oxygen ( $O_x = O_3 + NO_2$ ) was often used as  
537 an indicator of photochemical oxidant concentration in the atmosphere (Herndon et al.,  
538 2008; Hu et al., 2016; Wood et al., 2010). The diurnal variations of SOC and  $O_x$  mass  
539 concentrations in a one-hour resolution were plotted in Fig. 8. In this work, average  
540 SOC and  $O_x$  varied between  $1.8 \mu\text{gC}/\text{m}^3$  and  $8.8 \mu\text{gC}/\text{m}^3$ , and  $58 \mu\text{g}/\text{m}^3$  and  $214$   
541  $\mu\text{g}/\text{m}^3$ , respectively. The correlation coefficient (R) between SOC and  $O_x$  was 0.772  
542 (shown in Fig. S5), indicating that the SOC formation was associated with the  
543 photochemical oxidant concentration during this study.

544 Single particle mass spectrometry was also used to further investigate the mixing  
545 state and possible formation pathways of SOC. The relative peak area of  
546  $+43[\text{CH}_3\text{CO}^+/\text{CHNO}^+]$  during the daytime is a tracer of SOC formation (Qin et al.,  
547 2012; Zhang et al., 2014; Zhang et al., 2018). Time-series of hourly-averaged relative  
548 peak areas of  $m/z +43$  in ECOC type was shown in Fig. 9. Overall, the  $m/z +43$  curve  
549 peaked in the afternoon, which was consistent with the trend of  $O_x$ . This result  
550 indicates that SOC ( $m/z = +43$ ) produced by photochemical reactions condensed on  
551 BC particles. The average ECOC particle size verses time is also shown in Fig. 9. It  
552 peaked between 13:00 to 15:00 in the afternoon. Since the concentration of sulfate in  
553 the daytime was only slightly higher than that of nighttime (Fig. 8(c)), the increase of  
554 ECOC particle size was mainly caused by the condensation of SOC rather than  
555 secondary inorganic species. Therefore, in the afternoon, the intense photochemical  
556 process resulted in BC particles coated with more organic materials, leading to a  
557 increased coating thickness.

### 558 **3.3.3 Hygroscopicity and mixing state (coating material)**

559 As discussed above, the chemical composition measurement clearly shows BC  
 560 particles were coated with more SOC in the daytime and with more nitrate in the  
 561 nighttime. Sulfate concentration did not change much between daytime and nighttime.  
 562 Meanwhile, at a given GF, the coating for hygroscopic mode BC particles was thicker  
 563 in the daytime and thinner in the nighttime. The water uptake ability of nitrate is much  
 564 stronger than secondary organics. Thus, compared to SOC, less nitrate coating is  
 565 needed for a given hygroscopicity or GF.

566 To better understand this finding, we estimated volumes of different coating  
 567 materials required for a BC particle with a given hygroscopicity using the  
 568 Zdanovskii-Stokes-Robinson (ZSR) mixing rule (Stokes and Robinson, 1966),

$$569 \quad GF_{ZSR}(RH, D_p) = \left( \sum_i GF_i(RH, D_p)^3 \varepsilon_i \right)^{1/3} \quad (2)$$

570 The  $\varepsilon_i$  is the volume fractions of rBC, nitrate, sulfate, or organic coating in BC  
 571 particles. For simplicity, we assume rBC is covered by mixture containing either  
 572 SOC/(NH<sub>4</sub>)<sub>2</sub>SO<sub>4</sub> or (NH<sub>4</sub>)<sub>2</sub>SO<sub>4</sub>/NH<sub>4</sub>NO<sub>3</sub>, representing the mixing state of BC in  
 573 daytime and nighttime respectively. The GF for SOC is set to be 1.2, since Sjogren et  
 574 al. reported a uniform growth factor GF<sub>SOA</sub>=1.2 (RH = 90%) according to the ZSR  
 575 modelling results and field measurements (Sjogren et al., 2008). This value is at the  
 576 high end of previous measured SOA hygroscopicity range, thereby representing  
 577 highly aged and oxidized of SOA (Varutbangkul et al., 2006; Baltensperger et al.,  
 578 2005). The GFs of pure black carbon, (NH<sub>4</sub>)<sub>2</sub>SO<sub>4</sub>, and NH<sub>4</sub>NO<sub>3</sub> aerosol with a dry  
 579 size of 163 nm at RH=90% are calculated using the Aerosol Diameter-Dependent  
 580 Equilibrium Model (ADDEM) model. Their values are 1.0, 1.7 and 1.8 respectively  
 581 (Topping et al., 2005a, b).

582 For a coated BC particle with a dry diameter of 163 nm and a GF of 1.4, the  
 583 following relations would hold for SOC/(NH<sub>4</sub>)<sub>2</sub>SO<sub>4</sub> coating (eq. 3) and

584 (NH<sub>4</sub>)<sub>2</sub>SO<sub>4</sub>/NH<sub>4</sub>NO<sub>3</sub> coating (eq. 4):

585 
$$1.4 = \sqrt[3]{\varepsilon_{\text{BC}} \times \text{GF}_{\text{BC}}^3 + \varepsilon_{\text{SOC}} \times \text{GF}_{\text{SOC}}^3 + \varepsilon_{(\text{NH}_4)_2\text{SO}_4} \times \text{GF}_{(\text{NH}_4)_2\text{SO}_4}^3} \quad (3)$$

586 
$$1.4 = \sqrt[3]{\varepsilon'_{\text{BC}} \times \text{GF}_{\text{BC}}^3 + \varepsilon_{\text{NH}_4\text{NO}_3} \times \text{GF}_{\text{NH}_4\text{NO}_3}^3 + \varepsilon_{(\text{NH}_4)_2\text{SO}_4} \times \text{GF}_{(\text{NH}_4)_2\text{SO}_4}^3} \quad (4)$$

587  $\varepsilon_{\text{BC}}$  and  $\varepsilon'_{\text{BC}}$ , representing the volume fractions of rBC core in two mixing  
588 states, are given by  $\varepsilon_{\text{BC}} = 1 - \varepsilon_{\text{SOC}} - \varepsilon_{(\text{NH}_4)_2\text{SO}_4}$  and  $\varepsilon'_{\text{BC}} = 1 - \varepsilon_{\text{NH}_4\text{NO}_3} - \varepsilon_{(\text{NH}_4)_2\text{SO}_4}$ ,  
589 respectively. Here, we assume  $\varepsilon_{(\text{NH}_4)_2\text{SO}_4}$  is constant in both mixing states.

590 Combining equations above, the ratio of volume fraction of SOC to NH<sub>4</sub>NO<sub>3</sub> is

591 
$$\frac{\varepsilon_{\text{SOC}}}{\varepsilon_{\text{NH}_4\text{NO}_3}} = 6.6 \quad (5)$$

592 This calculation shows that higher volume fraction of SOC/(NH<sub>4</sub>)<sub>2</sub>SO<sub>4</sub> is needed for a  
593 BC particle to achieve the same GF as the one covered by (NH<sub>4</sub>)<sub>2</sub>SO<sub>4</sub>/NH<sub>4</sub>NO<sub>3</sub>.

594 This result confirms that different atmospheric aging pathways lead to changes in  
595 aerosol mixing state with distinct hygroscopicities: During nighttime with low  
596 temperature and high RH, formation or condensation of nitrates on BC particles  
597 enhanced the hygroscopicity of BC particles and resulted in the thinner coating BC  
598 particles in the hygroscopic mode for each selected size. During daytime,  
599 condensation of photo-chemically generated SOC on BC particles was associated to  
600 the thicker coating BC particles with less enhancement of hygroscopicity. The sulfate  
601 coating can enhance hygroscopicity of BC particles. However, unlike nitrate and SOC,  
602 its formation did not show a significant difference between day and night. **This**  
603 **finding is consistent with our previous measurement of secondary species formation**  
604 **in Shanghai during the summer time. Shanghai is a typical Chinese megacity with**  
605 **heavy air pollution. In summer, high NO<sub>x</sub> emission and ozone concentration led to**

606 enhanced nitrate formation via  $N_2O_5$  pathway during nighttime (Wang et al., 2009;  
607 Pathak et al., 2009). Secondary organic aerosol and particulate sulfate are usually  
608 formed through photo-oxidation of organic vapor and  $SO_2$  during daytime (Kroll and  
609 Seinfeld, 2008; Wang, et al., 2016). The differences in aging pathways between  
610 daytime and nighttime result in different coating materials and thickness on rBC cores,  
611 which can further impact their hygroscopicity. Noticeably, Liu et al., reports that the  
612 hygroscopicity of BC particles was largely driven by the coating of ammonium nitrate  
613 (Liu et al., 2013). However, it may not be the case in Shanghai during summer time,  
614 as most of particulate ammonium in Shanghai has been found to be in the form of  
615 ammonium sulfate (Wang et al., 2009; Pathak et al., 2009). Indeed, our SPAMS  
616 spectra for BC particles do not show the presence of large ammonium peaks (Fig. S2),  
617 because most of ammonium was in the form of ammonium sulfate, which is difficult  
618 to be ionized and detected in SPAMS (Wang et al., 2009).

619 Fig. 10 (a, b, and c) compares the coating thickness of 360 nm BC particles (GF  
620 = 1.4) with other chemical indicators, such as SOC, nitrate and sulfate. It shows that  
621 there was a positive correlation between the coating thickness and the SOC  
622 concentration and a negative correlation between the coating thickness and the nitrate  
623 concentration, which is consistent with their diurnal trends. There was a positive  
624 correlation between the coating thickness and sulfate concentration. Fig. 5(b) shows  
625 the coating thickness for 360 nm BC particles whose GF = 1.4 peaked in the  
626 afternoon. Formation of sulfate was also slightly enhanced during the afternoon due to  
627 stronger solar irradiation, resulting in this correlation.

628 Fig. 10(d, e, and f) shows the number fraction of BC particles in 360 nm aerosol  
629 of which GF is 1.4 verse the concentrations of SOC, nitrate and sulfate. It is found  
630 that the SOC had a negative correlation with the number fraction of BC particles in  
631 360 nm aerosol of which GF is 1.4, while nitrate and sulfate had a positive correlation  
632 with the number fraction. This finding is consistent with the fact that SOC has lower  
633 GF than nitrate and sulfate salts. When more SOC is formed and more likely covers

634 BC particles' surface, fewer BC particles' GF can reach 1.4. In contrast, when more  
635 nitrate or sulfate are formed and condense on BC particles, more BC particles' GF can  
636 reach 1.4.

#### 637 **4 Conclusions**

638 In this study, a HTDMA+SP2 system along with SPAMS were used to measure  
639 BC particles' hygroscopic properties in Shanghai during 2017's summer. Three  
640 hygroscopic modes, namely the hydrophobic mode, transition mode, and hydrophilic  
641 mode with GF at 1.0, 1.2, and 1.4, respectively, were selected to study the diurnal  
642 variations in rBC core and coating thickness as a function of time.

643 Our results reveal that the hygroscopicity of BC particle is determined by the  
644 coating layer thickness and materials, both of which are affected by atmospheric  
645 aging processes. For a specific BC particle size, a thin coating layer corresponded to  
646 freshly emitted BC particles with low hygroscopicity (e.g. GF=1.0). When BC  
647 particles became more hygroscopic (i.e. GF increases), the coating thickness  
648 increased. High yielding of particulate nitrate during nighttime was observed, and  
649 nitrate coating greatly enhanced the hygroscopicity of BC particles. During daytime,  
650 strong SOC formation from photochemical oxidation played an important role in the  
651 evolution of the BC mixing state. A thinner layer of nitrate coating could convert  
652 fresh BC particles to aged hygroscopic ones while a thicker coating layer of SOC and  
653 sulfate was required to reach the same overall hygroscopicity.

654 This study shows that atmospheric aging processes in a polluted city area play  
655 critical roles in the fast changing of aerosol mixing state during summer time. Time  
656 resolved information on particle hygroscopicity is necessary to evaluate the aging  
657 process, wet removal as well as climate effects of BC aerosols.

658

659 **Acknowledgements**

660 This work was supported by the National Natural Science Foundation of China (Nos.  
661 91544224, 41775150, 41827804, 21507010).

662

663 **References**

664 Allen, G. A., Lawrence, J., Koutrakis, P.: Field validation of a semi-continuous  
665 method for aerosol black carbon (aethalometer) and temporal patterns of  
666 summertime hourly black carbon measurements in southwestern PA, *Atmos.*  
667 *Environ.*, 33, 817–823, [https://doi.org/10.1016/S1352-2310\(98\)00142-3](https://doi.org/10.1016/S1352-2310(98)00142-3), 1999.

668 Andreae, M. O.: Soot carbon and excess fine potassium: Long-range transport of  
669 combustion-derived aerosols, *Science*, 220, 1148–1151,  
670 <https://doi.org/10.1126/science.220.4602.1148>, 1983.

671 Ault, A. P., Moore, M. J., Furutani, H., and Prather, K. A.: Impact of emissions from  
672 the Los Angeles port region on San Diego air quality during regional transport  
673 events, *Environ. Sci. Technol.*, 43, 3500–3506,  
674 <https://doi.org/10.1021/es8018918>, 2009.

675 Baltensperger, U., Kalberer, M., Dommen, J., Paulsen, D., Alfarra, M. R., Coe, H.,  
676 Fisseha, R., Gascho, A., Gysel, M., and Nyeki, S.: Secondary organic aerosols  
677 from anthropogenic and biogenic precursors, *Faraday Discussions*, 130, 265–278,  
678 <https://doi.org/10.1039/b417367h>, 2005.

679 Baumgardner, D., Kok, G., and Raga, G.: Warming of the Arctic lower stratosphere  
680 by light absorbing particles, *Geophys. Res. Lett.*, 31, L06117,  
681 <http://doi:10.1029/2003GL018883>, 2004.

682 Bhugwant, C., Cachier, H., Bessafi, M., Leveau, J.: Impact of traffic on black carbon  
683 aerosol concentration at la Reunion Island (Southern Indian Ocean), *Atmos.*  
684 *Environ.*, 34, 3463–3473, [https://doi.org/10.1016/S1352-2310\(99\)00405-7](https://doi.org/10.1016/S1352-2310(99)00405-7), 2000.

685 Bi, X., Zhang, G., Li, L., Wang, X., Li, M., Sheng, G., Fu, J., and Zhou, Z.: Mixing  
686 state of biomass burning particles by single particle aerosol mass spectrometer in  
687 the urban area of PRD, China, *Atmos. Environ.*, 45, 3447–3453,  
688 <https://doi.org/10.1016/j.atmosenv.2011.03.034>, 2011.

689 Bond, T. C. and Bergstrom, R. W.: Light absorption by carbonaceous particles: An  
690 investigative review, *Aerosol Sci. Tech.*, 40, 27–67,  
691 <http://doi:10.1080/02786820500421521>, 2006.

692 Bond, T. C., Doherty, S. J., Fahey, D., Forster, P., Berntsen, T., DeAngelo, B.,  
693 Flanner, M., Ghan, S., Kärcher, B., and Koch, D.: Bounding the role of black  
694 carbon in the climate system: A scientific assessment, *J. Geophys. Res. Atmos.*,  
695 118, 5380–5552, <https://doi.org/10.1002/jgrd.50171>, 2013.

696 Cao, J.-J., Zhu, C.-S., Tie, X.-X., Geng, F.-H., Xu, H.-M., Ho, S., Wang, G.-H., Han,  
697 Y.-M., and Ho, K.-F.: Characteristics and sources of carbonaceous aerosols from  
698 Shanghai, China, *Atmos. Chem. Phys.*, 13, 803–817,  
699 <https://doi.org/10.5194/acp-13-803-2013>, 2013.

700 Change, I. P. o. C.: Climate change 2014: mitigation of climate change, Cambridge  
701 University Press, 2015.

702 Chen, J., Zhao, C., Ma, N., Liu, P., Göbel, T., Hallbauer, E., Deng, Z., Ran, L., Xu,  
703 W., and Liang, Z.: A parameterization of low visibilities for hazy days in the  
704 North China Plain, *Atmos. Chem. Phys.*, 12, 4935–4950,  
705 <https://doi.org/10.5194/acp-12-4935-2012>, 2012.

706 Chirico, R., DeCarlo, P., Heringa, M., Tritscher, T., Richter, R., Prévôt, A., Dommen,  
707 J., Weingartner, E., Wehrle, G., and Gysel, M.: Impact of aftertreatment devices  
708 on primary emissions and secondary organic aerosol formation potential from  
709 in-use diesel vehicles: results from smog chamber experiments, *Atmos. Chem.*  
710 *Phys.*, 10, 11545–11563, <https://doi.org/10.5194/acp-10-11545-2010>, 2010.

711 Chou, C.-K., Lee, C., Cheng, M., Yuan, C., Chen, S., Wu, Y., Hsu, W., Lung, S., Hsu,  
712 S., and Lin, C.: Seasonal variation and spatial distribution of carbonaceous  
713 aerosols in Taiwan, *Atmos. Chem. Phys.*, 10, 9563–9578,  
714 <https://doi.org/10.5194/acp-10-9563-2010>, 2010.

715 Dall'Osto, M., and Harrison, R. M.: Chemical characterisation of single airborne  
716 particles in Athens (Greece) by ATOFMS, *Atmos. Environ.*, 40, 7614–7631,  
717 <https://doi.org/10.1016/j.atmosenv.2006.06.053>, 2006.

718 DeCarlo, P. F., Slowik, J. G., Worsnop, D. R., Davidovits, P. and Jimenez, J. L.:  
719 Particle morphology and density characterization by combined mobility and  
720 aerodynamic diameter measurements. Part 1: theory. *Aerosol Sci. Technol.*, 38,  
721 <http://doi:10.1080/027868290903907>, 2004.

722 Dreher, D. B., Harley, R. A.: A fuel-based inventory for heavy-duty diesel truck  
723 emissions, *J. Air Waste Manage.*, 48, 352–358,  
724 <https://doi.org/10.1080/10473289.1998.10463686>, 1998.

725 Du, H., Kong, L., Cheng, T., Chen, J., Yang, X., Zhang, R., Han, Z., Yan, Z., and Ma,  
726 Y.: Insights into ammonium particle-to-gas conversion: non-sulfate ammonium  
727 coupling with nitrate and chloride, *Aerosol Air Qual. Res.*, 10, 589–595,  
728 <https://doi.org/10.4209/aaqr.2010.04.0034>, 2010.

- 729 Dusek, U., Reischl, G. P., and Hitzenberger, R.: CCN activation of pure and coated  
730 carbon black particles, *Environ. Sci. Technol.*, 40, 1223–1230,  
731 <http://doi:10.1021/es0503478>, 2006.
- 732 Gao, R., Schwarz, J., Kelly, K., Fahey, D., Watts, L., Thompson, T., Spackman, J.,  
733 Slowik, J., Cross, E., and Han, J. H.: A novel method for estimating  
734 light-scattering properties of soot aerosols using a modified single-particle soot  
735 photometer, *Aerosol Sci. Tech.*, 41, 125–135,  
736 <https://doi.org/10.1080/02786820601118398>, 2007.
- 737 Gong, X., Zhang, C., Chen, H., Nizkorodov, S. A., Chen, J., and Yang, X.: Size  
738 distribution and mixing state of black carbon particles during a heavy air  
739 pollution episode in Shanghai, *Atmos. Chem. Phys.*, 16, 5399–5411,  
740 <https://doi.org/10.5194/acp-16-5399-2016>, 2016.
- 741 Gysel, M., Nyeki, S., Weingartner, E., Baltensperger, U., Giebl, H., Hitzenberger, R.,  
742 Petzold, A., and Wilson, C. W.: Properties of jet engine combustion particles  
743 during the PartEmis experiment: Hygroscopicity at subsaturated conditions,  
744 *Geophys. Res. Lett.*, 30, 1566, <https://doi:10.1029/2003GL016896>, 2003.
- 745 Harris, S. J., and Maricq, M. M.: Signature size distributions for diesel and gasoline  
746 engine exhaust particulate matter, *J. Aerosol Sci.*, 32, 749–764,  
747 [https://doi.org/10.1016/S0021-8502\(00\)00111-7](https://doi.org/10.1016/S0021-8502(00)00111-7), 2001.
- 748 Healy, R. M., Sciare, J., Poulain, L., Kamili, K., Merkel, M., Müller, T.,  
749 Wiedensohler, A., Eckhardt, S., Stohl, A., and Sarda-Estève, R.: Sources and  
750 mixing state of size-resolved elemental carbon particles in a European megacity:  
751 Paris, *Atmos. Chem. Phys.*, 12, 1681–1700,  
752 <https://doi.org/10.5194/acp-12-1681-2012>, 2012.

753 Heintzenberg, J., and Covert, D. S.: On the distribution of physical and chemical  
754 particle properties in the atmospheric aerosol, *J. Atmos. Chem.*, 10, 383–397,  
755 <https://link.springer.com/article/10.1007/BF00115781>, 1990.

756 Herich, H., Kammermann, L., Gysel, M., Weingartner, E., Baltensperger, U.,  
757 Lohmann, U., and Cziczo, D. J.: In situ determination of atmospheric aerosol  
758 composition as a function of hygroscopic growth, *J. Geophys. Res. Atmos.*, 113,  
759 D16213, <https://doi.org/10.1029/2008JD009954>, 2008.

760 Heringa, M., DeCarlo, P., Chirico, R., Tritscher, T., Dommen, J., Weingartner, E.,  
761 Richter, R., Wehrle, G., Prévôt, A., and Baltensperger, U.: Investigations of  
762 primary and secondary particulate matter of different wood combustion  
763 appliances with a high-resolution time-of-flight aerosol mass spectrometer,  
764 *Atmos. Chem. Phys.*, 11, 5945–5957, <https://doi.org/10.5194/acp-11-5945-2011>,  
765 2011.

766 Herndon, S. C., Onasch, T. B., Wood, E. C., Kroll, J. H., Canagaratna, M. R., Jayne, J.  
767 T., Zavala, M. A., Knighton, W. B., Mazzoleni, C., and Dubey, M. K.:  
768 Correlation of secondary organic aerosol with odd oxygen in Mexico City,  
769 *Geophys. Res. Lett.*, 35, L15804, <https://doi.org/10.1029/2008GL034058>, 2008.

770 Hu, W., Hu, M., Hu, W., Jimenez, J. L., Yuan, B., Chen, W., Wang, M., Wu, Y.,  
771 Chen, C., and Wang, Z.: Chemical composition, sources, and aging process of  
772 submicron aerosols in Beijing: Contrast between summer and winter, *J. Geophys.*  
773 *Res. Atmos.*, 121, 1955–1977, <https://doi.org/10.1002/2015JD024020>, 2016.

774 Huang, X.-F., Sun, T.-L., Zeng, L.-W., Yu, G.-H., and Luan, S.-J.: Black carbon  
775 aerosol characterization in a coastal city in South China using a single particle  
776 soot photometer, *Atmos. Environ.*, 51, 21–28,  
777 <https://doi.org/10.1016/j.atmosenv.2012.01.056>, 2012.

778 Huang, Y., Li, L., Li, J., Wang, X., Chen, H., Chen, J., Yang, X., Gross, D., Wang, H.,  
779 and Qiao, L.: A case study of the highly time-resolved evolution of aerosol  
780 chemical and optical properties in urban Shanghai, China, *Atmos. Chem. Phys.*,  
781 13, 3931–3944, <https://doi.org/10.5194/acp-13-3931-2013>, 2013.

782 Johnson, G. R., Ristovski, Z. D., D’Anna, B., and Morawska, L.: Hygroscopic  
783 behavior of partially volatilized coastal marine aerosols using the volatilization  
784 and humidification tandem differential mobility analyzer technique. *J. Geophys.*  
785 *Res.*, 110, D20203, <https://doi:10.1029/2004JD005657>, 2005.

786 Kondo, Y., Komazaki, Y., Miyazaki, Y., Moteki, N., Takegawa, N., Kodama, D.,  
787 Deguchi, S., Nogami, M., Fukuda, M., and Miyakawa, T.: Temporal variations  
788 of elemental carbon in Tokyo, *J. Geophys. Res. Atmos.*, 111, D12205,  
789 <https://doi.org/10.1029/2005JD006257>, 2006.

790 Kondo, Y.: Effects of black carbon on climate: Advances in measurement and  
791 modeling, *Monographs on Environment, Environ. Earth Planets*, 3, 1–85,  
792 <https://doi.org/10.5047/meep.2015.00301.0001>, 2015.

793 Kuwata, M., Kondo, Y., Mochida, M., Takegawa, N., and Kawamura, K.:  
794 Dependence of CCN activity of less volatile particles on the amount of coating  
795 observed in Tokyo, *J. Geophys. Res.*, 112, D11207,  
796 <https://doi:10.1029/2006JD007758>, 2007.

797 Kuwata, M. and Kondo, Y.: Dependence of size-resolved CCN spectra on the mixing  
798 state of nonvolatile cores observed in Tokyo, *J. Geophys. Res.*, 113, D19202,  
799 <http://doi:10.1029/2007JD009761>, 2008.

800 Kroll, J. H., and Seinfeld, J. H.: Chemistry of secondary organic aerosol: Formation  
801 and evolution of low-volatility organics in the atmosphere, *Atmos. Environ.*, 42,  
802 3593–3624, <https://doi.org/10.1016/j.atmosenv.2008.01.003>, 2008.

803 Löndahl, J., Massling, A., Pagels, J., Swietlicki, E., Vaclavik, E., and Loft, S.:  
804 Size-resolved respiratory-tract deposition of fine and ultrafine hydrophobic and  
805 hygroscopic aerosol particles during rest and exercise, *Inhal. Toxicol.*, 19, 109–  
806 116, <https://doi.org/10.1080/08958370601051677>, 2007.

807 Laborde, M., Crippa, M., Tritscher, T., Jurányi, Z., Decarlo, P., Temime-Roussel, B.,  
808 Marchand, N., Eckhardt, S., Stohl, A., and Baltensperger, U.: Black carbon  
809 physical properties and mixing state in the European megacity Paris, *Atmos.*  
810 *Chem. Phys.*, 13, 5831–5856, <https://doi.org/10.5194/acp-13-5831-2013>, 2013.

811 Lammel, G. and Novakov, T.: Water nucleation properties of carbon-black and diesel  
812 soot particles, *Atmos. Environ.*, 29, 813–823, 1995.

813 Leskinen, A. P., Jokiniemi, J. K., and Lehtinen, K. E.: Characterization of aging wood  
814 chip combustion aerosol in an environmental chamber, *Atmos. Environ.*, 41,  
815 3713–3721, <https://doi.org/10.1016/j.atmosenv.2006.12.016>, 2007.

816 Lewis, K. A., Arnott, W. P., Moosmuller, H., Chakrabarty, R. K., and Mishchenko, M.  
817 I.: Reduction in biomass burning aerosol light absorption upon humidification:  
818 roles of inorganically-induced hygroscopicity, particle collapse, and  
819 photoacoustic heat and mass transfer, *Atmos. Chem. Phys.*, 9, 8949–8966,  
820 <http://doi:10.5194/acp-9-8949-2009>, 2009.

821 Li, H., Zhang, Q., Zhang, Q., Chen, C., Wang, L., Wei, Z., Zhou, S., Parworth, C.,  
822 Zheng, B., and Canonaco, F.: Wintertime aerosol chemistry and haze evolution  
823 in an extremely polluted city of the North China Plain: significant contribution  
824 from coal and biomass combustion, *Atmos. Chem. Phys.*, 17, 4751–4768,  
825 <https://doi.org/10.5194/acp-17-4751-2017>, 2017.

826 Li, L., Huang, Z., Dong, J., Li, M., Gao, W., Nian, H., Fu, Z., Zhang, G., Bi, X., and  
827 Cheng, P.: Real time bipolar time-of-flight mass spectrometer for analyzing

828 single aerosol particles, *Int. J. Mass Spectrom.*, 303, 118–124,  
829 <https://doi.org/10.1016/j.ijms.2011.01.017>, 2011.

830 Liu, D., Allan, J., Whitehead, J., Young, D., Flynn, M., Coe, H., McFiggans, G.,  
831 Fleming, Z. L., and Bandy, B.: Ambient black carbon particle hygroscopic  
832 properties controlled by mixing state and composition, *Atmos. Chem. Phys.*, 13,  
833 2015–2029, <https://doi.org/10.5194/acp-13-2015-2013>, 2013.

834 Liu, D., Allan, J. D., Young, D. E., Coe, H., Beddows, D., Fleming, Z. L., Prevot, A.  
835 S.: Size distribution, mixing state and source apportionment of black carbon  
836 aerosol in London during wintertime, *Atmos. Chem. Phys.*, 14, 10061–10084,  
837 <https://doi.org/10.5194/acp-14-10061-2014>, 2014.

838 Matsui, H., Koike, M., Kondo, Y., Moteki, N., Fast, J. D., and Zaveri, R. A.:  
839 Development and validation of a black carbon mixing state resolved three -  
840 dimensional model: Aging processes and radiative impact, *J. Geophys. Res.*  
841 *Atmos.*, 118, 2304–2326, <https://doi.org/10.1029/2012JD018446>, 2013.

842 McMeeking, G. R., Hamburger, T., Liu, D., Flynn, M., Morgan, W. T., Northway, M.,  
843 Highwood, E. J., Krejci, R., Allan, J. D., Minikin, A., and Coe, H.: Black carbon  
844 measurements in the boundary layer over western and northern Europe, *Atmos.*  
845 *Chem. Phys.*, 10, 9393–9414, <http://doi:10.5194/acp-10-9393-2010>, 2010.

846 McMeeking, G., Good, N., Petters, M., McFiggans, G., and Coe, H.: Influences on the  
847 fraction of hydrophobic and hydrophilic black carbon in the atmosphere, *Atmos.*  
848 *Chem. Phys.*, 11, 5099–5112, <https://doi.org/10.5194/acp-11-5099-2011>, 2011.

849 Moffet, R., Foy, B. d., Molina, L. a., Molina, M., and Prather, K.: Measurement of  
850 ambient aerosols in northern Mexico City by single particle mass spectrometry,  
851 *Atmos. Chem. Phys.*, 8, 4499–4516, <https://doi.org/10.5194/acp-8-4499-2008>,  
852 2008.

853 Mogili, P. K., Kleiber, P. D., Young, M. A., and Grassian, V. H.: N<sub>2</sub>O<sub>5</sub> hydrolysis on  
854 the components of mineral dust and sea salt aerosol: Comparison study in an  
855 environmental aerosol reaction chamber, *Atmos. Environ.*, 40, 7401–7408,  
856 <https://doi.org/10.1016/j.atmosenv.2006.06.048>, 2006.

857 Moteki, N. and Kondo, Y.: Dependence of laser-induced incandescence on physical  
858 properties of black carbon aerosols: Measurements and theoretical interpretation,  
859 *Aerosol Sci. Tech.*, 44, 663–675, <https://doi.org/10.1080/02786826.2010.484450>,  
860 2010.

861 Mozurkewich, M., Calvert, J. G.: Reaction probability of N<sub>2</sub>O<sub>5</sub> on aqueous aerosols, *J.*  
862 *Geophys. Res. Atmos.*, 93, 15889–15896,  
863 <https://doi.org/10.1029/JD093iD12p15889>, 1988.

864 Notario, A., Bravo, I., Adame, J. A., Díaz-de-Mera, Y., Aranda, A., Rodríguez, A.,  
865 and Rodríguez, D.: Analysis of NO, NO<sub>2</sub>, NO<sub>x</sub>, O<sub>3</sub> and oxidant (O<sub>x</sub>= O<sub>3</sub>+ NO<sub>2</sub>)  
866 levels measured in a metropolitan area in the southwest of Iberian Peninsula,  
867 *Atmos. Res.*, 104, 217–226, <https://doi.org/10.1016/j.atmosres.2011.10.008>,  
868 2012.

869 Pagels, J., Khalizov, A. F., McMurry, P. H., and Zhang, R. Y.: Processing of soot by  
870 controlled sulphuric acid and water condensation-Mass and mobility  
871 relationships, *Aerosol Sci. Technol.*, 43, 629–640,  
872 <https://doi.org/10.1080/02786820902810685>, 2009.

873 Pathak, R. K., Wu, W. S., Wang, T.: Summertime PM<sub>2.5</sub> ionic species in four major  
874 cities of China: nitrate formation in an ammonia-deficient atmosphere, *Atmos.*  
875 *Chem. Phys.*, 9, 1711–1722, <https://doi.org/10.5194/acp-9-1711-2009>, 2009.

876 Petzold, A., Gysel, M., Vancassel, X., Hitzenberger, R., Puxbaum, H., Vrochticky, S.,  
877 Weingartner, E., Baltensperger, U., and Mirabel, P.: On the effects of organic

878 matter and sulphur containing compounds on the CCN activation of combustion  
879 particles, *Atmos. Chem. Phys.*, 5, 3187–3203,  
880 <https://doi:10.5194/acp-5-3187-2005>, 2005.

881 Pratt, K., Murphy, S., Subramanian, R., DeMott, P., Kok, G., Campos, T., Rogers, D.,  
882 Prenni, A., Heymsfield, A., and Seinfeld, J.: Flight-based chemical  
883 characterization of biomass burning aerosols within two prescribed burn smoke  
884 plumes, *Atmos. Chem. Phys.*, 11, 12549–12565,  
885 <https://doi.org/10.5194/acp-11-12549-2011>, 2011.

886 Qin, X., Pratt, K. A., Shields, L. G., Toner, S. M., and Prather, K. A.: Seasonal  
887 comparisons of single-particle chemical mixing state in Riverside, CA, *Atmos.*  
888 *Environ.*, 59, 587–596, <https://doi.org/10.1016/j.atmosenv.2012.05.032>, 2012.

889 Reid, J., Koppmann, R., Eck, T., and Eleuterio, D.: A review of biomass burning  
890 emissions part II: intensive physical properties of biomass burning particles,  
891 *Atmos. Chem. Phys.*, 5, 799–825, <https://doi.org/10.5194/acp-5-799-2005>, 2005.

892 Riemer, N., Vogel, H., & Vogel, B.: Soot aging time scales in polluted regions during  
893 day and night, *Atmos. Chem. Phys.*, 4, 1885–1893,  
894 <https://doi.org/10.5194/acp-4-1885-2004>, 2004.

895 Rose, D., Gunthe, S. S., Su, H., Garland, R. M., Yang, H., Berghof, M., Cheng, Y. F.,  
896 Wehner, B., Achtert, P., Nowak, A., Wiedensohler, A., Takegawa, N., Kondo, Y.,  
897 Hu, M., Zhang, Y., Andreae, M. O., and Poschl, U.: Cloud condensation nuclei  
898 in polluted air and biomass burning smoke near the megacity Guangzhou,  
899 China-Part 2: Size-resolved aerosol chemical composition, diurnal cycles, and  
900 externally mixed weakly CCN-active soot particles, *Atmos. Chem. Phys.*, 11,  
901 2817–2836, <https://doi:10.5194/acp-11-2817-2011>, 2011.

902 Schneider, J., Hock, N., Weimer, S., Borrmann, S., Kirchner, U., Vogt, R., and Scheer,  
903 V.: Nucleation particles in diesel exhaust: Composition inferred from in situ  
904 mass spectrometric analysis, *Environ. Sci. Technol.*, 39, 6153–6161,  
905 <https://doi.org/10.1021/es049427m>, 2005.

906 Schwarz, J. P., Gao, R. S., Fahey, D. W., Thomson, D. S., Watts, L. A., Wilson, J. C.,  
907 Reeves, J. M., Darbeheshti, M., Baumgardner, D. G., Kok, G. L., Chung, S. H.,  
908 Schulz, M., Hendricks, J., Lauer, A., Karcher, B., Slowik, J. G., Rosenlof, K. H.,  
909 Thompson, T. L., Langford, A. O., Loewenstein, M., and Aikin, K. C.:  
910 Single-particle measurements of midlatitude black carbon and light-scattering  
911 aerosols from the boundary layer to the lower stratosphere, *J. Geophys. Res.*, 111,  
912 D16207, <http://doi:10.1029/2006JD007076>, 2006.

913 Shiraiwa, M., Kondo, Y., Moteki, N., Takegawa, N., Miyazaki, Y., and Blake, D.:  
914 Evolution of mixing state of black carbon in polluted air from Tokyo, *Geophys.*  
915 *Res. Lett.*, 34, L16803, <https://doi.org/10.1029/2007GL029819>, 2007.

916 Sjogren, S., Gysel, M., Weingartner, E., Alfarra, M., Duplissy, J., Cozic, J., Crosier, J.,  
917 Coe, H., and Baltensperger, U.: Hygroscopicity of the submicrometer aerosol at  
918 the high-alpine site Jungfraujoch, 3580 m asl, Switzerland, *Atmos. Chem. Phys.*,  
919 8, 5715–5729, <https://doi.org/10.5194/acp-8-5715-2008>, 2008.

920 Slowik, J. G., Stainken, K., Davidovits, P., Williams, L., Jayne, J., Kolb, C., Worsnop,  
921 D. R., Rudich, Y., DeCarlo, P. F., and Jimenez, J. L.: Particle morphology and  
922 density characterization by combined mobility and aerodynamic diameter  
923 measurements. Part 2: Application to combustion-generated soot aerosols as a  
924 function of fuel equivalence ratio, *Aerosol Sci. Tech.*, 38, 1206–1222,  
925 <https://doi.org/10.1080/027868290903916>, 2004.

926 Song, X.-H., Hopke, P. K., Fergenson, D. P., and Prather, K. A.: Classification of  
927 single particles analyzed by ATOFMS using an artificial neural network,  
928 ART-2A, *Anal. Chem.*, 71, 860–865, [https://doi.org/ 10.1021/ac9809682](https://doi.org/10.1021/ac9809682), 1999.

929 Soto-Garcia, L. L., Andreae, M. O., Andreae, T. W., Artaxo, P., Maenhaut, W.,  
930 Kirchstetter, T., Novakov, T., Chow, J. C., and Mayol-Bracero, O. L.: Evaluation  
931 of the carbon content of aerosols from the burning of biomass in the Brazilian  
932 Amazon using thermal, optical and thermal-optical analysis methods, *Atmos.*  
933 *Chem. Phys.*, 11, 4425–4444, <https://doi.org/10.5194/acp-11-4425-2011>, 2011.

934 Spencer, M. T., Shields, L. G., and Prather, K. A.: Simultaneous measurement of the  
935 effective density and chemical composition of ambient aerosol particles, *Environ.*  
936 *Sci. Technol.*, 41, 1303–1309, <https://doi.org/10.1021/es061425+>, 2007.

937 Stokes, R., and Robinson, R.: Interactions in aqueous nonelectrolyte solutions. I.  
938 Solute-solvent equilibria, *J. Phys. Chem.*, 70, 2126–2131,  
939 <https://doi.org/10.1021/j100879a010>, 1966.

940 Swietlicki, E., HANSSON, H. C., Hämeri, K., Svenningsson, B., Massling, A.,  
941 McFiggans, G., McMurry, P., Petäjä, T., Tunved, P., and Gysel, M.:  
942 Hygroscopic properties of submicrometer atmospheric aerosol particles  
943 measured with H - TDMA instruments in various environments—A review,  
944 *Tellus B*, 60, 432–469, <https://doi.org/10.1111/j.1600-0889.2008.00350.x>, 2008.

945 Topping, D., McFiggans, G., and Coe, H.: A curved multi-component aerosol  
946 hygroscopicity model framework: Part 2—Including organic compounds, *Atmos.*  
947 *Chem. Phys.*, 5, 1223–1242, <https://doi.org/10.5194/acp-5-1223-2005>, 2005a.

948 Topping, D., McFiggans, G., and Coe, H.: A curved multi-component aerosol  
949 hygroscopicity model framework: Part 1—Inorganic compounds, *Atmos. Chem.*  
950 *Phys.*, 5, 1205–1222, <https://doi.org/10.5194/acp-5-1205-2005>, 2005b.

- 951 Varutbangkul, V., Brechtel, F., Bahreini, R., Ng, N., Keywood, M., Kroll, J., Flagan,  
952 R., Seinfeld, J., Lee, A., and Goldstein, A.: Hygroscopicity of secondary organic  
953 aerosols formed by oxidation of cycloalkenes, monoterpenes, sesquiterpenes, and  
954 related compounds, *Atmos. Chem. Phys.*, 6, 2367–2388,  
955 <https://doi.org/10.5194/acp-6-2367-2006>, 2006.
- 956 Wang, D., Zhou, B., Fu, Q., Zhao, Q., Zhang, Q., Chen, J., Yang, X., Duan, Y., and Li,  
957 J.: Intense secondary aerosol formation due to strong atmospheric photochemical  
958 reactions in summer: observations at a rural site in eastern Yangtze River Delta  
959 of China, *Sci. Total Environ.*, 571, 1454–1466,  
960 <https://doi.org/10.1016/j.scitotenv.2016.06.212>, 2016a.
- 961 Wang, Q., Huang, R.-J., Zhao, Z., Zhang, N., Wang, Y., Ni, H., Tie, X., Han, Y.,  
962 Zhuang, M., and Wang, M.: Size distribution and mixing state of refractory black  
963 carbon aerosol from a coastal city in South China, *Atmos. Res.*, 181, 163–171,  
964 <https://doi.org/10.1016/j.atmosres.2016.06.022>, 2016b.
- 965 Wang, X., Zhang, Y., Chen, H., Yang, X., Chen, J., and Geng, F.: Particulate nitrate  
966 formation in a highly polluted urban area: a case study by single-particle mass  
967 spectrometry in Shanghai, *Environ. Sci. Technol.*, 43, 3061–3066,  
968 <https://doi.org/10.1021/es8020155>, 2009.
- 969 Wang, X., Williams, B. J., Wang, X., Tang, Y., Huang, Y., Kong, L., Yang, X., and  
970 Biswas, P.: Characterization of organic aerosol produced during pulverized coal  
971 combustion in a drop tube furnace, *Atmos. Chem. Phys.*, 13, 10919–10932,  
972 <https://doi.org/10.5194/acp-13-10919-2013>, 2013.
- 973 Wang, X., Ye, X., Chen, H., Chen, J., Yang, X., and Gross, D. S.: Online  
974 hygroscopicity and chemical measurement of urban aerosol in Shanghai, China,  
975 *Atmos. Environ.*, 95, 318–326, <https://doi.org/10.1016/j.atmosenv.2014.06.051>,  
976 2014.

977 Weingartner, E., Burtscher, H., and Baltensperger, U.: Hygroscopic properties of  
978 carbon and diesel soot particles, *Atmos. Environ.*, 31, 2311–2327,  
979 [https://doi.org/10.1016/S1352-2310\(97\)00023-X](https://doi.org/10.1016/S1352-2310(97)00023-X), 1997.

980 Winkler, P.: The growth of atmospheric aerosol particles as a function of the relative  
981 humidity—II. An improved concept of mixed nuclei, *J. Aerosol Sci.*, 4, 373–387,  
982 [https://doi.org/10.1016/0021-8502\(73\)90027-X](https://doi.org/10.1016/0021-8502(73)90027-X), 1973.

983 Wood, E., Canagaratna, M., Herndon, S., Onasch, T., Kolb, C., Worsnop, D., Kroll, J.,  
984 Knighton, W., Seila, R., and Zavala, M.: Investigation of the correlation between  
985 odd oxygen and secondary organic aerosol in Mexico City and Houston, *Atmos.*  
986 *Chem. Phys.*, 10, 8947–8968, <https://doi.org/10.5194/acp-10-8947-2010>, 2010.

987 Xue, J., Li, Y., Wang, X., Durbin, T.D., Johnson, K.C., Karavalakis, G., Asa-Awuku,  
988 A., Villela, M., Quiros, D., Hu, S. and Huai, T.: Comparison of vehicle exhaust  
989 particle size distributions measured by SMPS and EEPS during steady-state  
990 conditions, *Aerosol Sci. Tech.*, 49, 984–996, [https://doi:](https://doi.org/10.1080/02786826.2015.1088146)  
991 [10.1080/02786826.2015.1088146](https://doi.org/10.1080/02786826.2015.1088146), 2015.

992 Ye, X., Chen, T., Hu, D., Yang, X., Chen, J., Zhang, R., Khakuziv, A. F., and Wang,  
993 L.: A multifunctional HTDMA system with a robust temperature control, *Adv.*  
994 *Atmos. Sci.*, 26, 1235–1240, <https://doi.org/10.1007/s00376-009-8134-3>, 2009.

995 Ye, X., Tang, C., Yin, Z., Chen, J., Ma, Z., Kong, L., Yang, X., Gao, W., and Geng,  
996 F.: Hygroscopic growth of urban aerosol particles during the 2009  
997 Mirage-Shanghai Campaign, *Atmos. Environ.*, 64, 263–269,  
998 <https://doi.org/10.1016/j.atmosenv.2012.09.064>, 2013.

999 Zervas, E., and Dorlhene, P.: Comparison of exhaust particle number measured by  
1000 EEPS, CPC, and ELPI, *Aerosol Sci. Technol.*, 40, 977–984,  
1001 <https://doi.org/10.1080/02786820600844093>, 2006.

1002 Zhai, J., Lu, X., Li, L., Zhang, Q., Zhang, C., Chen, H., Yang, X., and Chen, J.:  
1003 Size-resolved chemical composition, effective density, and optical properties of  
1004 biomass burning particles, *Atmos. Chem. Phys.*, 17, 7481–7493,  
1005 <https://doi.org/10.5194/acp-17-7481-2017>, 2017.

1006 Zhang, C., Lu, X., Zhai, J., Chen, H., Yang, X., Zhang, Q., Zhao, Q., Fu, Q., Sha, F.,  
1007 and Jin, J.: Insights into the formation of secondary organic carbon in the  
1008 summertime in urban Shanghai, *J. Environ. Sci.*, article in press  
1009 <https://doi.org/10.1016/j.jes.2017.12.018>, 2018.

1010 Zhang, G., Bi, X., He, J., Chen, D., Chan, L. Y., Xie, G., Wang, X., Sheng, G., Fu, J.,  
1011 and Zhou, Z.: Variation of secondary coatings associated with elemental carbon  
1012 by single particle analysis, *Atmos. Environ.*, 92, 162–170,  
1013 <https://doi.org/10.1016/j.atmosenv.2014.04.018>, 2014.

1014 Zhang, R. Y., Khalizov, A. F., Pagels, J., Zhang, D., Xue, H., and McMurry, P. H.:  
1015 Variability in morphology, hygroscopicity, and optical properties of soot  
1016 aerosols during atmospheric processing, *P. Natl. Acad. Sci. USA*, 105, 10291–  
1017 10296, <http://doi:10.1073/pnas.0804860105>, 2008.

1018

1019

**Table 1.** Number counts and fractions of the five types of BC-containing particles detected by the SPAMS.

Type	Number count of particles	Fraction of particles
Pure EC	5191	8.1%
KEC	21456	33.3%
NaKEC	11001	17.1%
ECOC	21225	33.0%
Others	5495	8.5%
Total BC-containing particles	64368	100%

1020

1021

1022

1023

1024

1025

1026

1027

1028

1029

1030

1031 **Figure Captions**

1032 **Figure 1.** Schematic diagram of experimental setup.

1033 **Figure 2.** Temporal profiles of gaseous pollutants ( $O_3$ ,  $SO_2$ ,  $CO$ , and  $NO_2$ ),  
1034 temperature, relative humidity (RH), and  $PM_{2.5}$  and  $PM_{10}$  mass concentrations.

1035 **Figure 3.** Averaged hygroscopic growth distributions of **(a)** total ambient particles  
1036 and **(b)** BC particles at RH = 85% for three selected sizes ( $D_0=120$  nm, 240 nm and  
1037 360 nm).

1038 **Figure 4.** Diurnal variations of BC **(a)** number concentration and **(b)** number fraction  
1039 (the ratio of the number concentration of BC particles to that of total particles at a  
1040 certain  $D_0$  and GF) for three selected size.

1041 **Figure 5.** Diurnal variations of rBC **(a)** core size and **(b)** coating thickness at different  
1042 GFs.

1043 **Figure 6.** Diurnal variations of the GF distribution for BC particles. The BC aerosol  
1044 number fraction for each GF is defined as (BC aerosol number concentration for this  
1045 GF)/(sum of BC aerosol number concentration for GF = 1.0, 1.2 and 1.4).

1046 **Figure 7.** Diurnal variations of number fraction of each classified particle type: **(a)**  
1047  $G_{200-400}$ :  $200 < d_{va} < 400$  nm and **(b)**  $G_{400-800}$ :  $400 < d_{va} < 800$  nm.

1048 **Figure 8.** Averaged diurnal variations of  $O_x$ , SOC,  $SO_4^{2-}$  and  $NO_3^-$  mass  
1049 concentration in **(a)**, **(b)**, **(c)** and **(d)**, respectively. The blue line in **(d)** is daily  
1050 variation of relative peak area of  $NO_3^-$  measured by SPAMS.

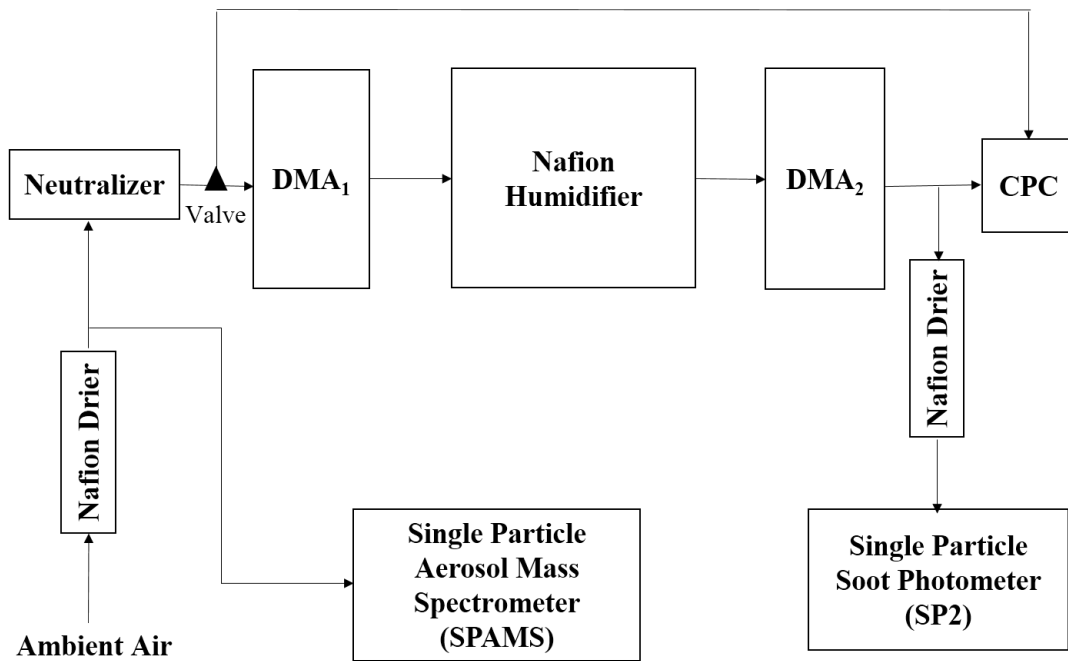
1051 **Figure 9.** Diurnal variations of relative peak area (RPA) of  $m/z +43$  from ECOC type  
1052 particles and the average aerodynamic particle size of ECOC particles.

1053 **Figure 10.** Relations between the coating thickness of 360 nm BC particles of which  
1054 GF is 1.4 and the concentration of **(a)** SOC, **(b)** nitrate and **(c)** sulfate; Relations

1055 between the number fraction of BC particles in 360 nm aerosol of which GF is 1.4  
1056 and the concentration of (d) SOC, (e) nitrate and (f) sulfate.

1057

1058



1059

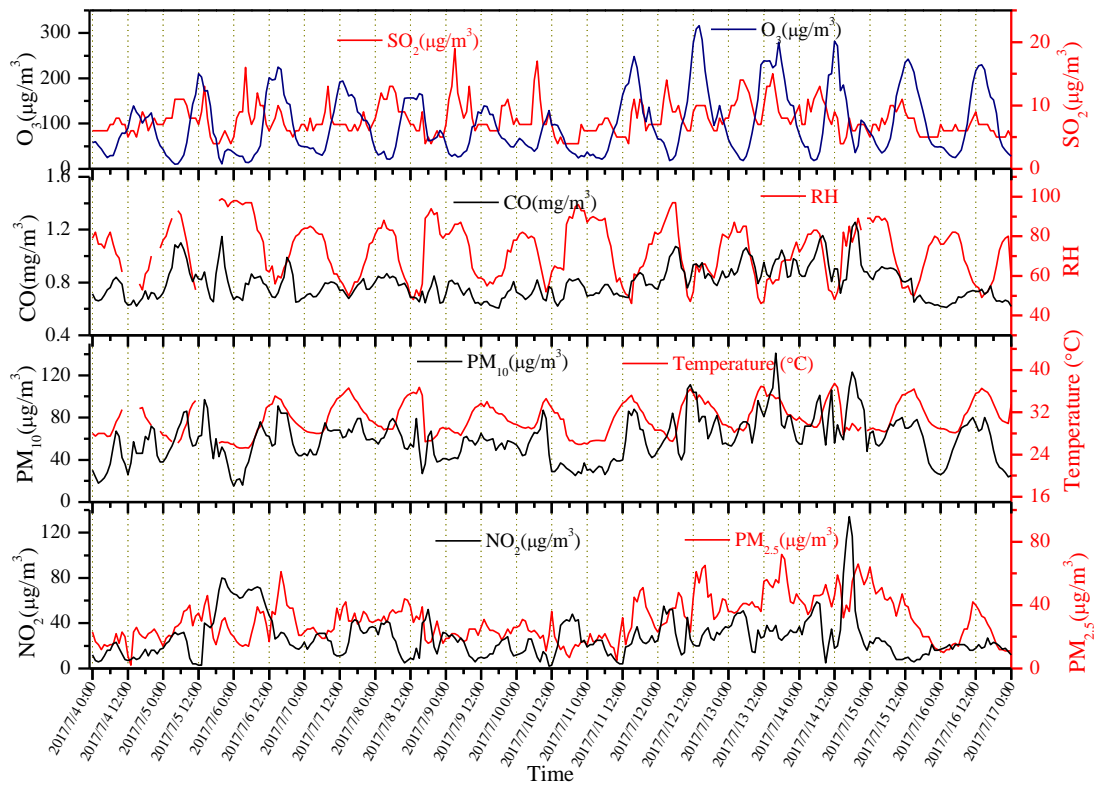
1060

**Figure 1.** Schematic diagram of experimental setup.

1061

1062

1063

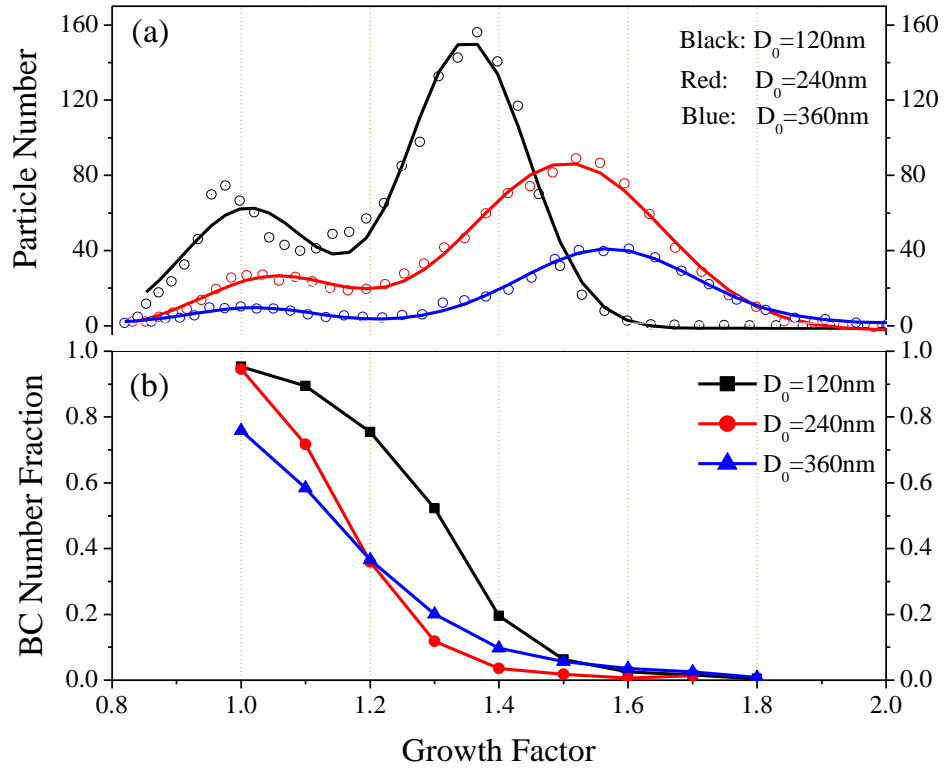


1064

1065

1066 **Figure 2.** Temporal profiles of gaseous pollutants ( $O_3$ ,  $SO_2$ ,  $CO$ , and  $NO_2$ ),  
 1067 temperature, relative humidity (RH), and  $PM_{2.5}$  and  $PM_{10}$  mass concentrations.

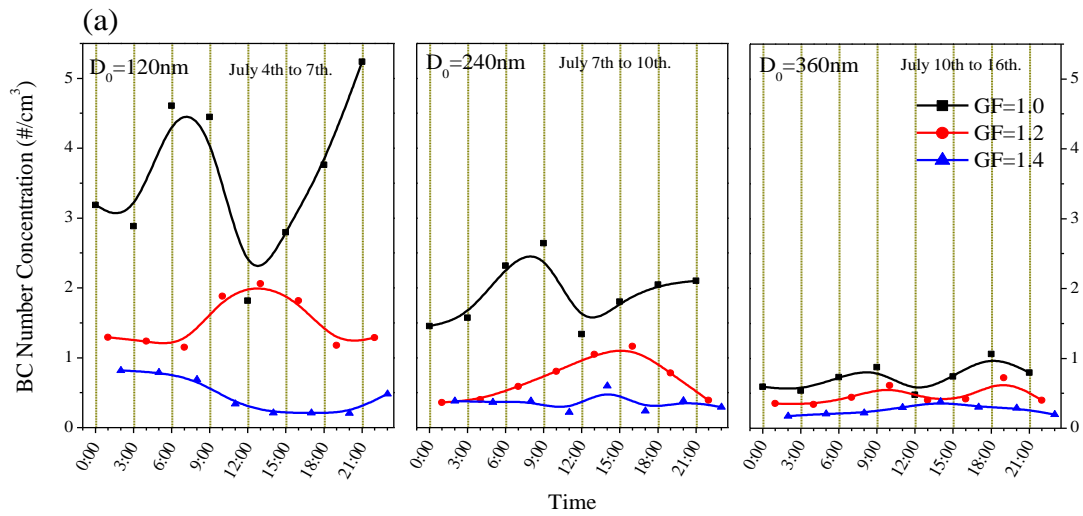
1068



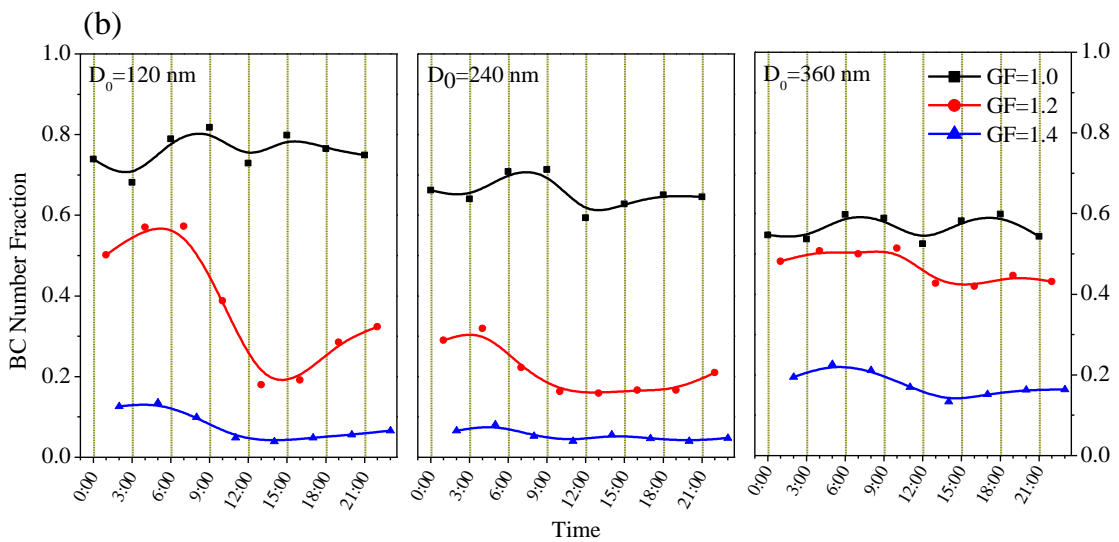
1069  
1070

1071 **Figure 3.** Averaged hygroscopic growth distributions of (a) total ambient particles and  
1072 (b) BC particles at RH = 85% for three selected sizes ( $D_0=120$  nm, 240 nm and 360  
1073 nm).

1074  
1075  
1076

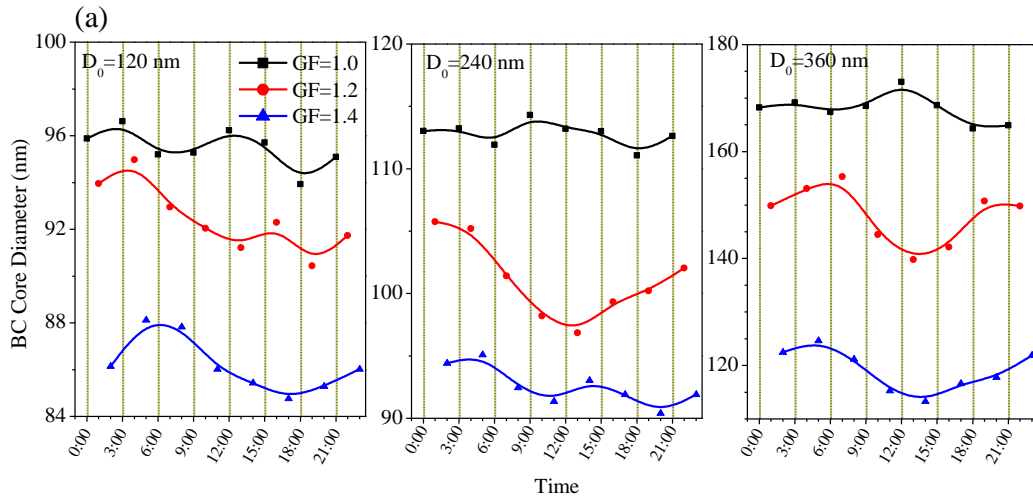


1077

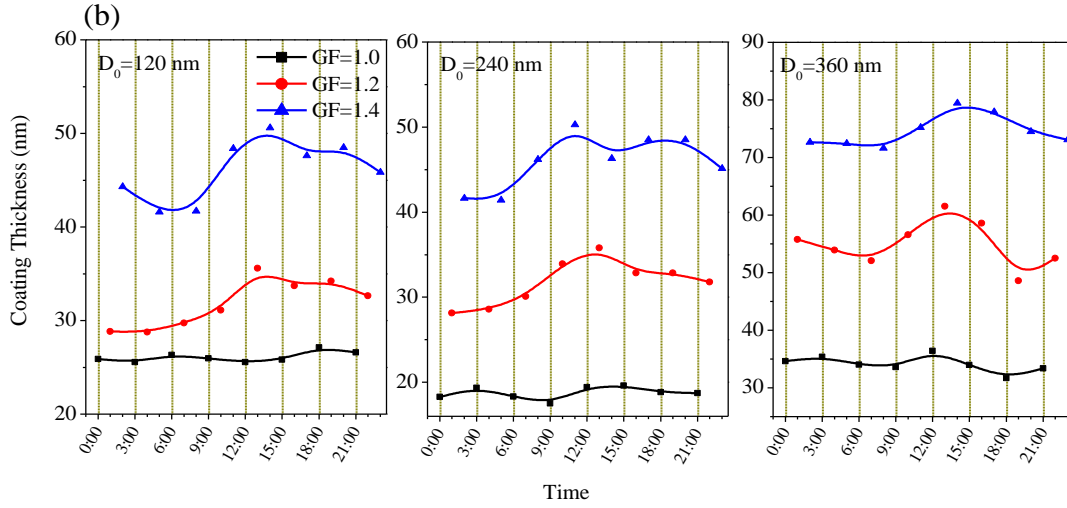


1078

1079 **Figure 4.** Diurnal variations of BC **(a)** number concentration and **(b)** number fraction  
 1080 (the ratio of the number concentration of BC particles to that of total particles at a  
 1081 certain  $D_0$  and GF) for three selected size.



1082



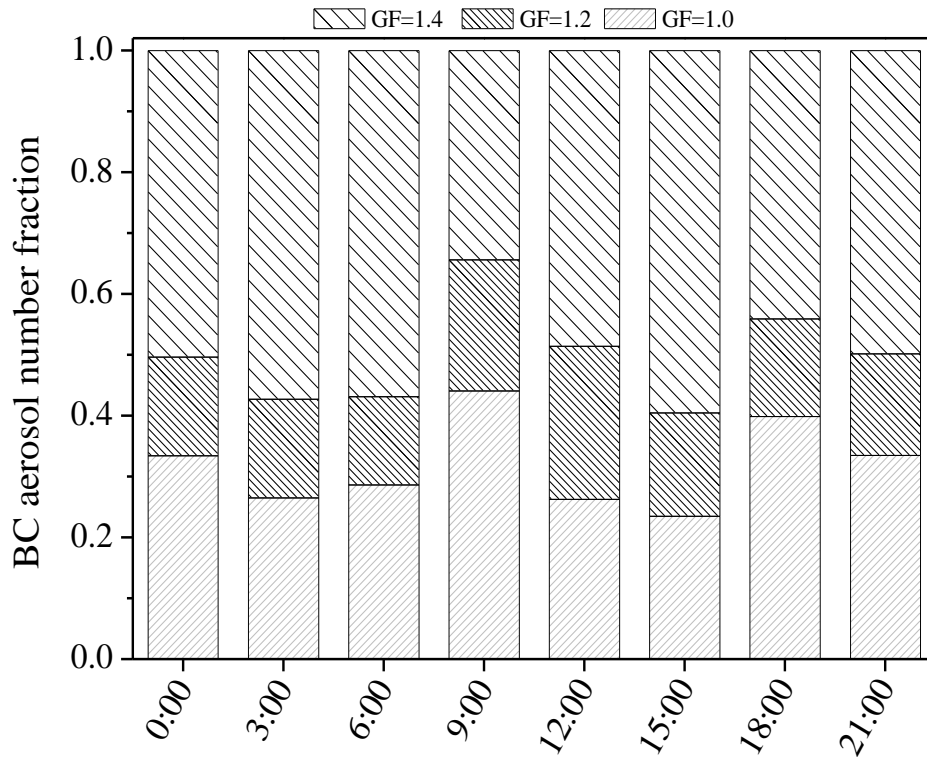
1083

1084

1085 **Figure 5.** Diurnal variations of rBC (a) core size and (b) coating thickness at different

1086 GFs.

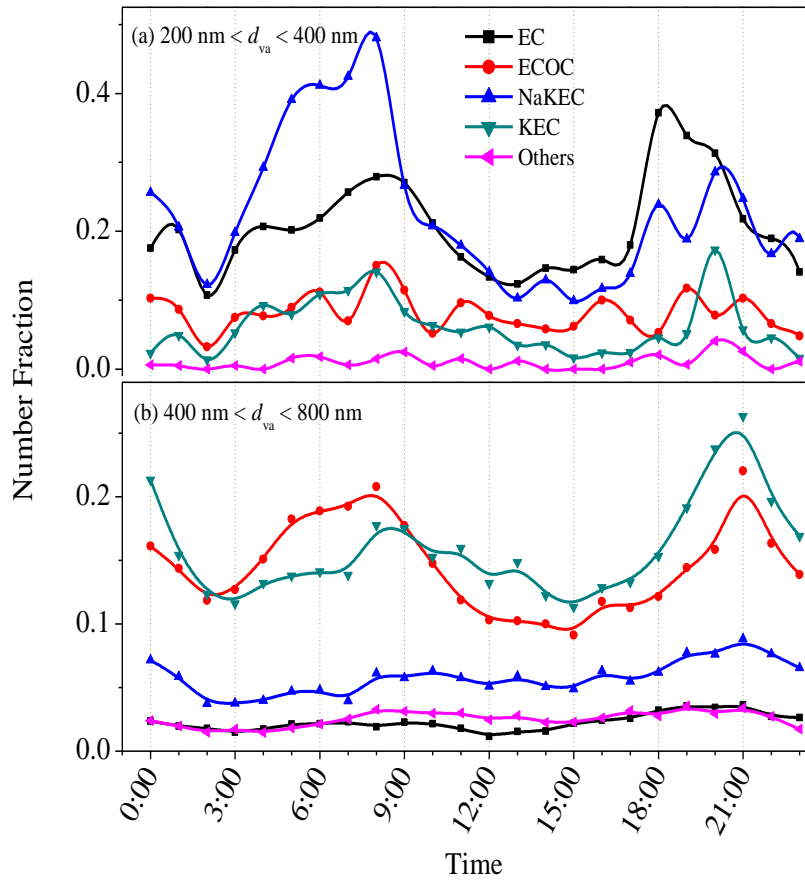
1087



1088

1089 **Figure 6.** Diurnal variations of the GF distribution for BC particles. The BC aerosol  
 1090 number fraction for each GF is defined as (BC aerosol number concentration for this  
 1091 GF)/(sum of BC aerosol number concentration for GF = 1.0, 1.2 and 1.4).

1092



1093

1094

1095 **Figure 7.** Diurnal variations of number fraction of each classified particle type: **(a)**

1096  $G_{200-400}$ :  $200 < d_{va} < 400 \text{ nm}$  and **(b)**  $G_{400-800}$ :  $400 < d_{va} < 800 \text{ nm}$ .

1097

1098

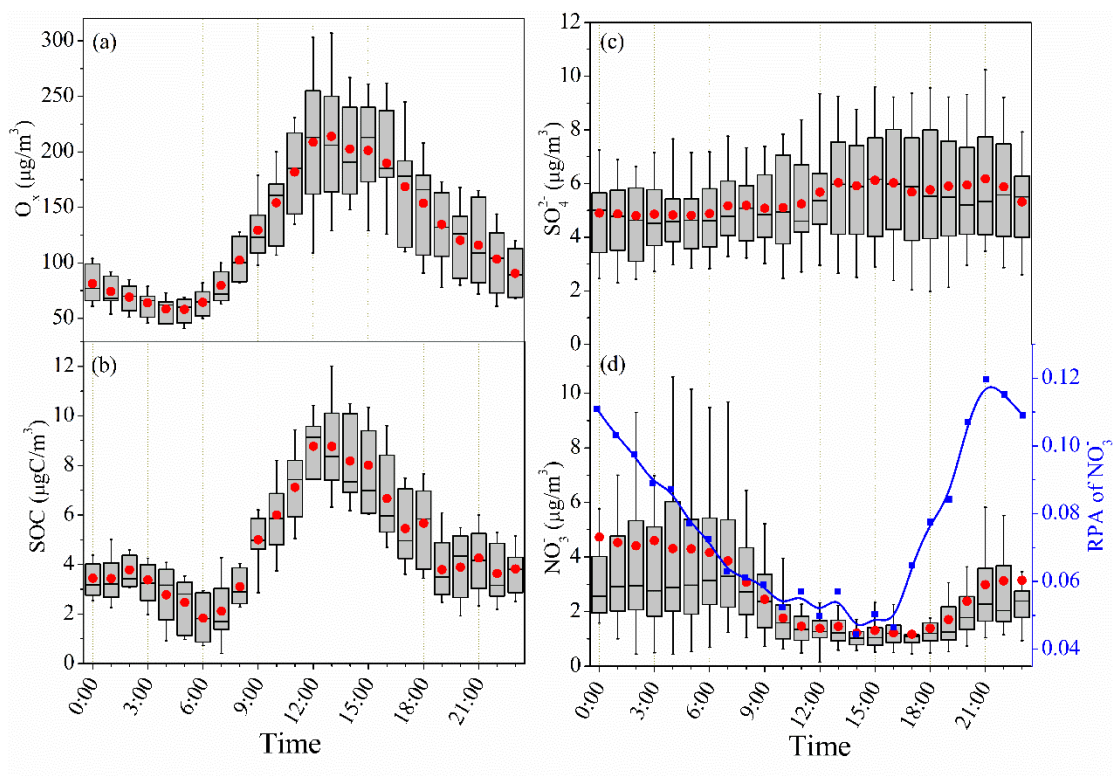
1099

1100

1101

1102

1103

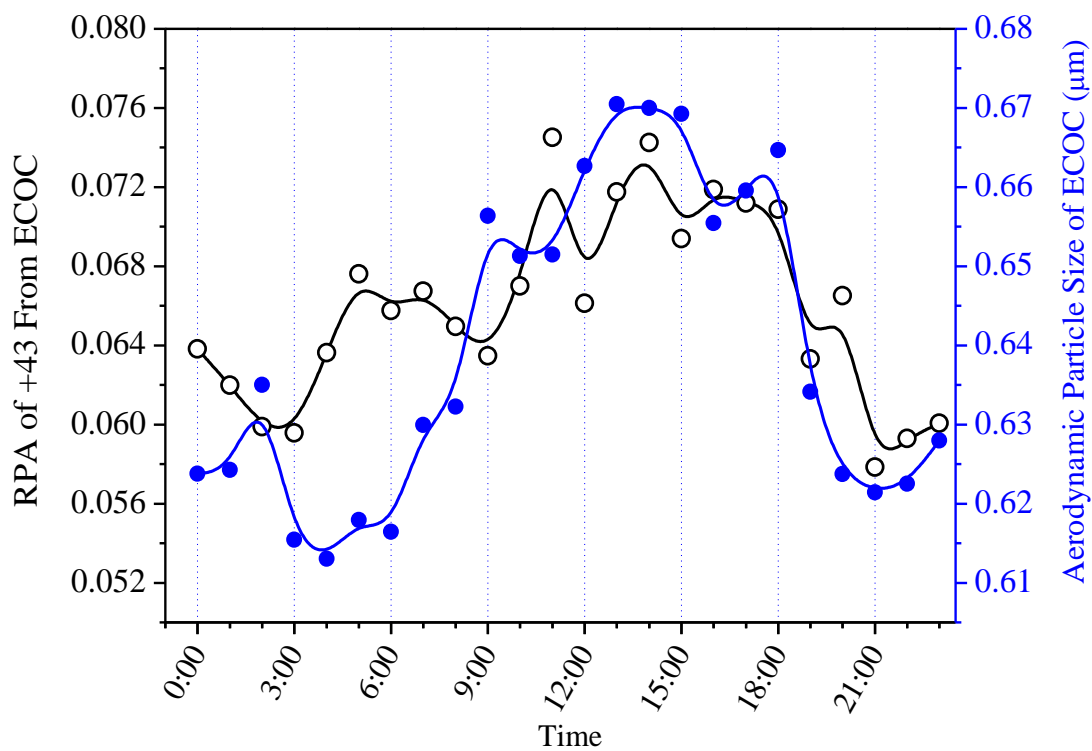


1104

1105 **Figure 8.** Averaged diurnal variations of  $O_x$ , SOC,  $SO_4^{2-}$  and  $NO_3^-$  mass  
 1106 concentration in (a), (b), (c) and (d), respectively. The blue line in (d) is daily  
 1107 variation of relative peak area (RPA) of  $NO_3^-$  measured by SPAMS.

1108

1109



1110  
1111

1112 **Figure 9.** Diurnal variations of relative peak area (RPA) of m/z +43 from ECOC type  
1113 particles and the average aerodynamic particle size of ECOC particles.

1114

1115

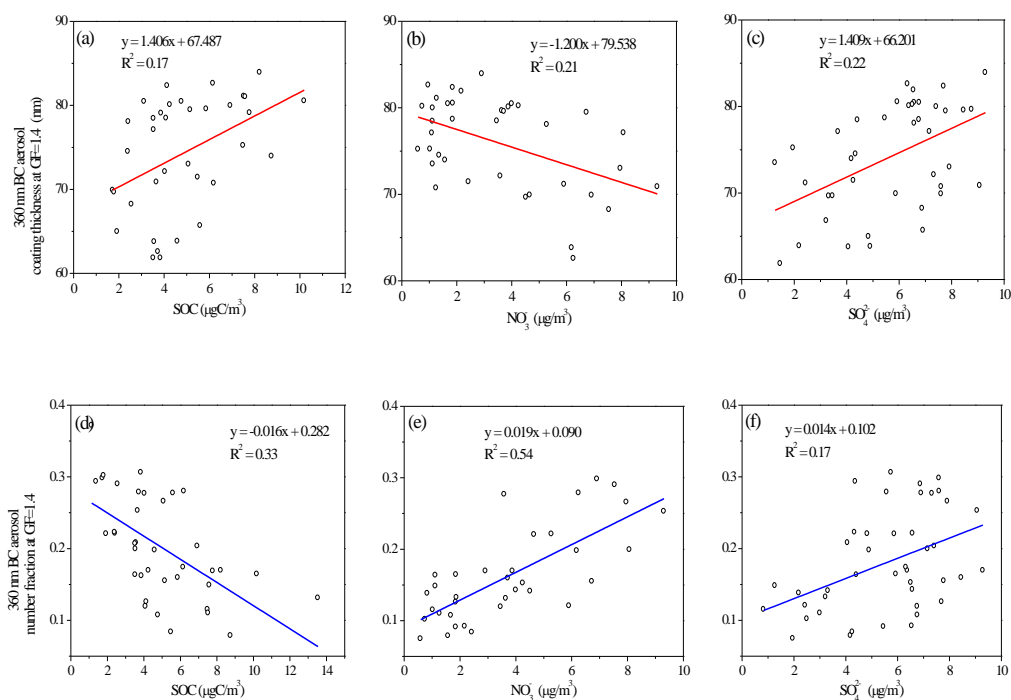
1116

1117

1118

1119

1120



1121

1122 **Figure 10.** Relations between the coating thickness of 360 nm BC particles of which  
 1123 GF is 1.4 and the concentration of (a) SOC, (b) nitrate and (c) sulfate; Relations  
 1124 between the number fraction of BC particles in 360 nm aerosol of which GF is 1.4  
 1125 and the concentration of (d) SOC, (e) nitrate and (f) sulfate.

1126

1127

1128

1129

1130

1131

1132

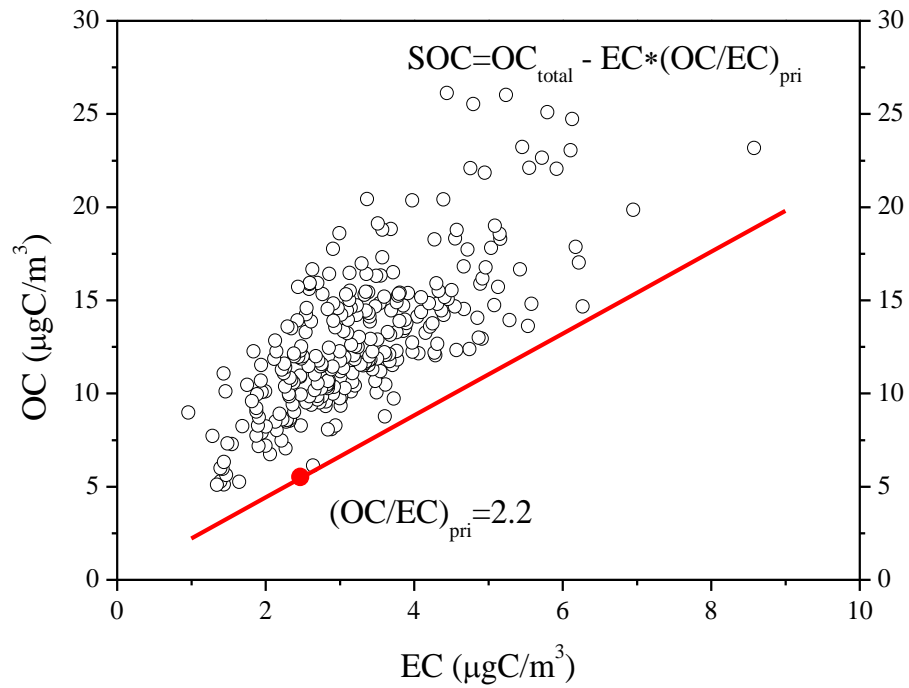
1133

1134

1135

1136 **Supplementary information**

1137



1138

1139

1140 **Figure S1.** The scattering plot for the measured OC and EC concentration. The red  
1141 line represents the minimum value of OC/EC ratio.

1142

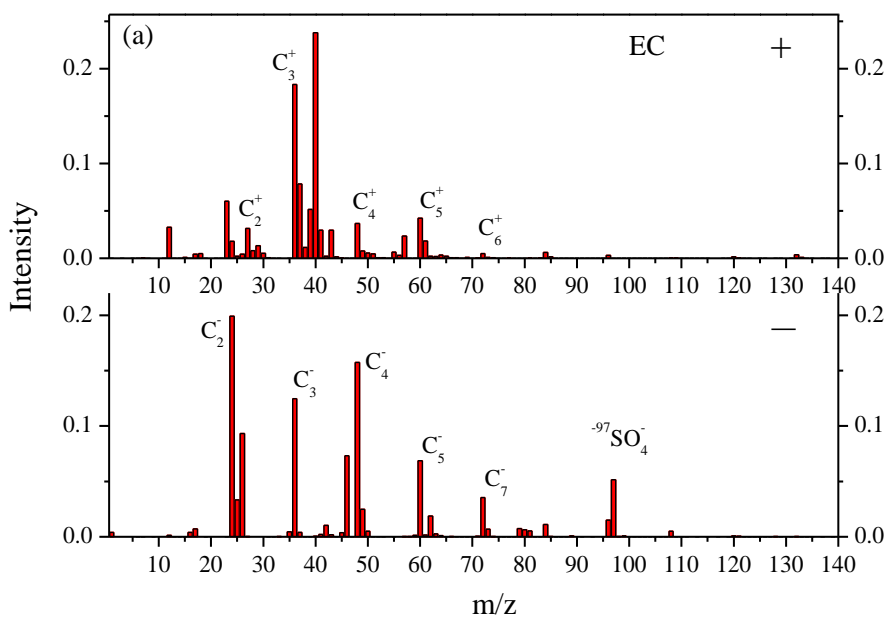
1143

1144

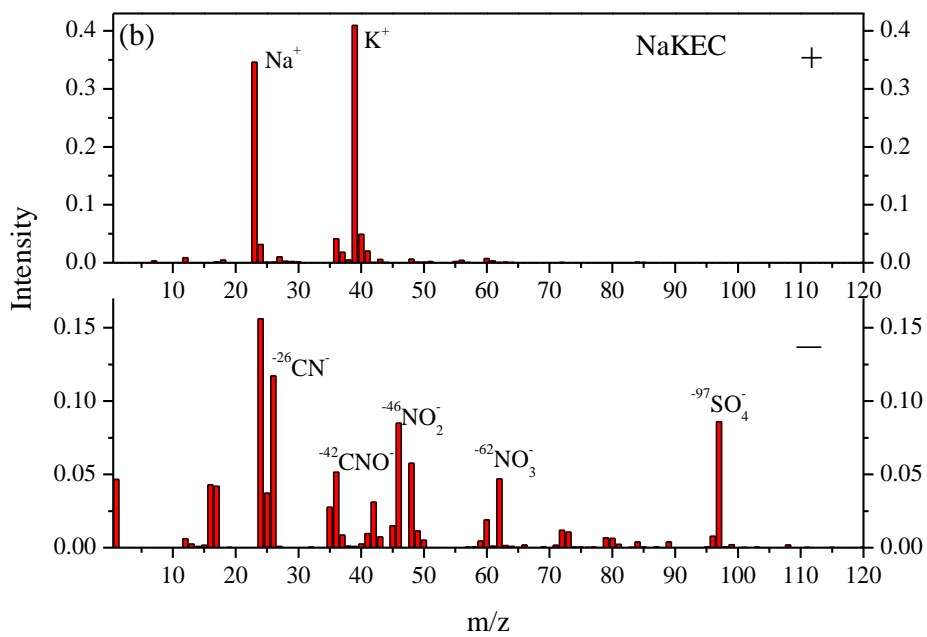
1145

1146

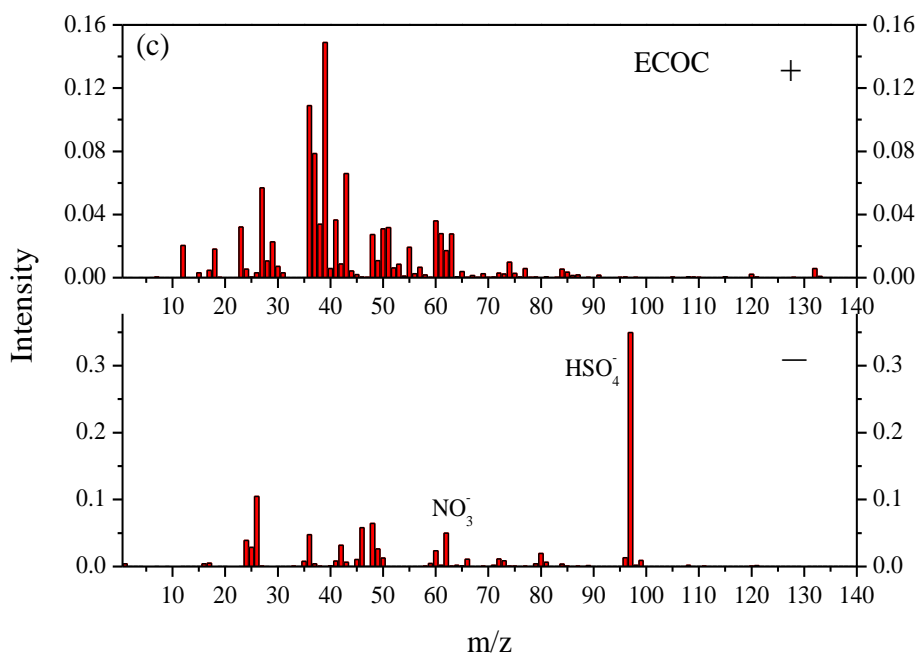
1147



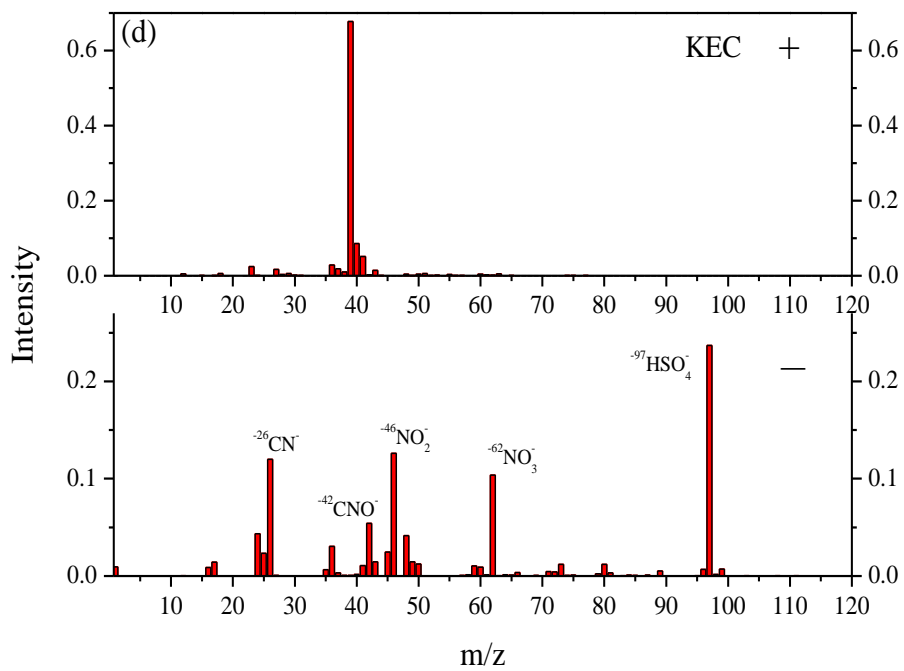
1148



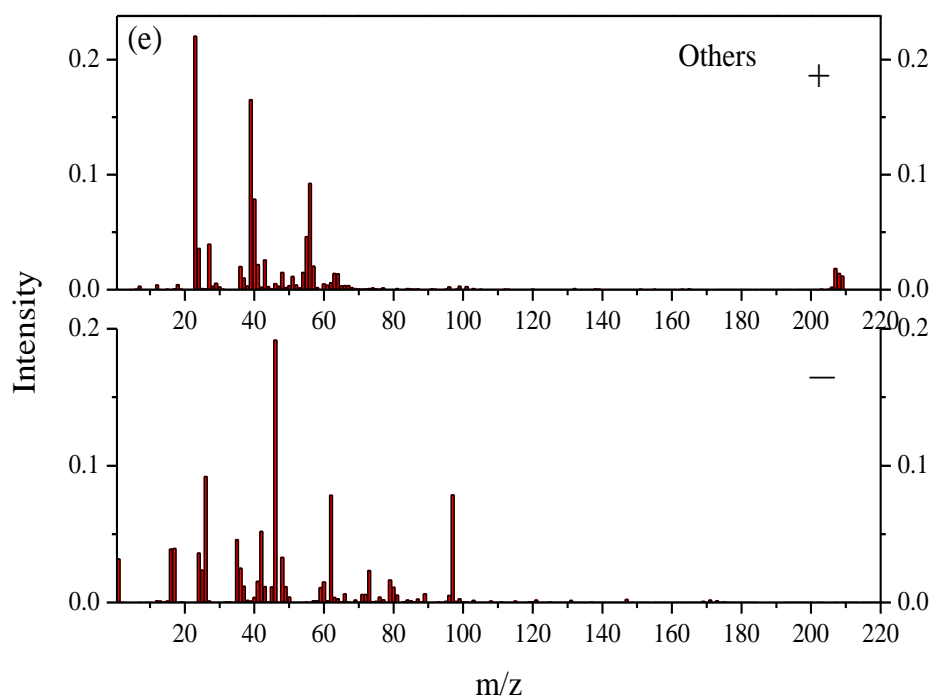
1149



1150



1151



1152

1153 **Figure S2.** Averaged mass spectra of different types of BC-containing particles: (a)  
 1154 EC; (b) NaKEC; (c) ECOC; (d) KEC; (e) Others (the unit for the intensity is  
 1155 arbitrary).

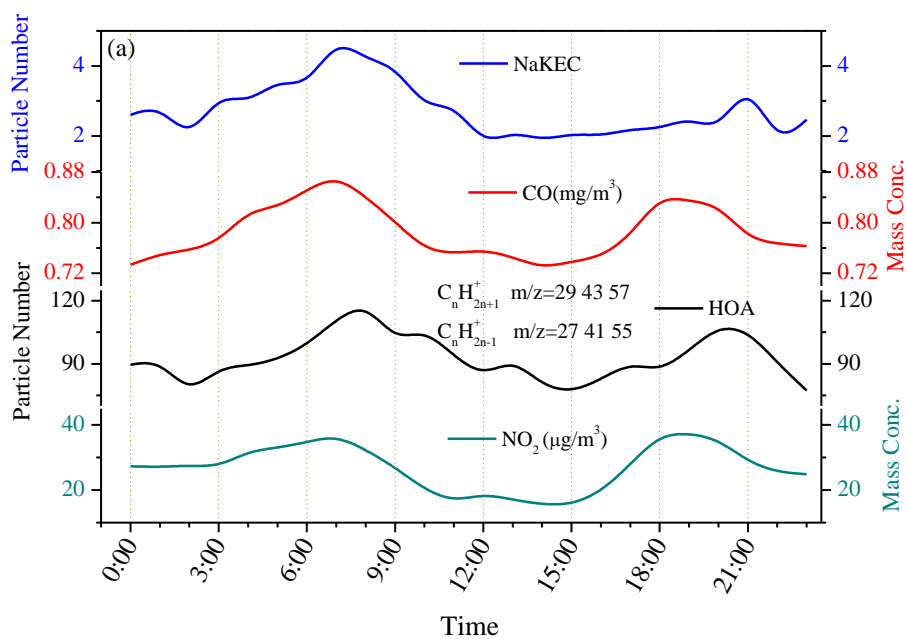
1156

1157

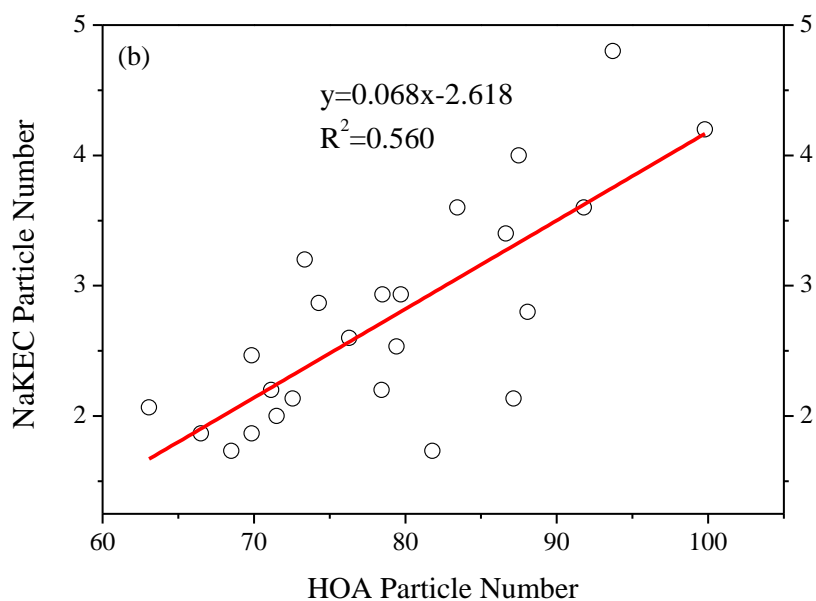
1158

1159

1160



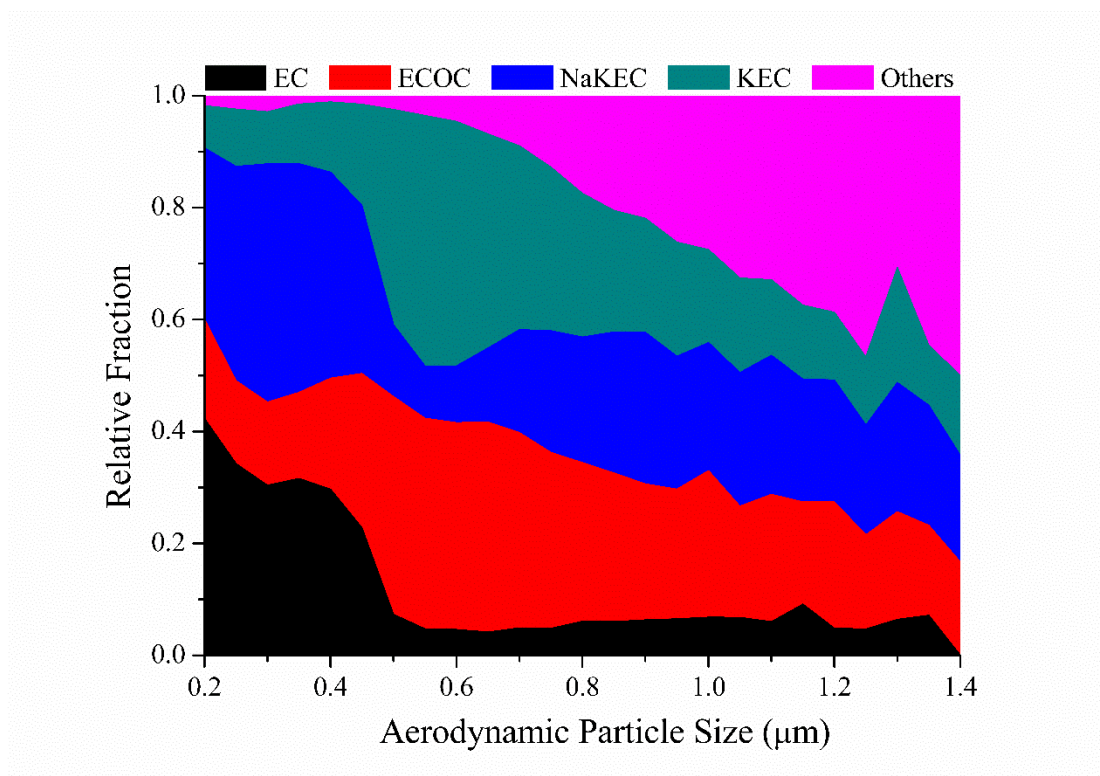
1161



1162

1163 **Figure S3.** (a) Diurnal variation of NaKEC and HOA particle number sampled by  
 1164 SPAMS, as well as CO and NO<sub>2</sub> concentrations; (b) Correlation between NaKEC and  
 1165 HOA particles.

1166



1167

1168 **Figure S4.** Relative fractions of five particle types as a function of particle size  
 1169 measured by SPAMS.

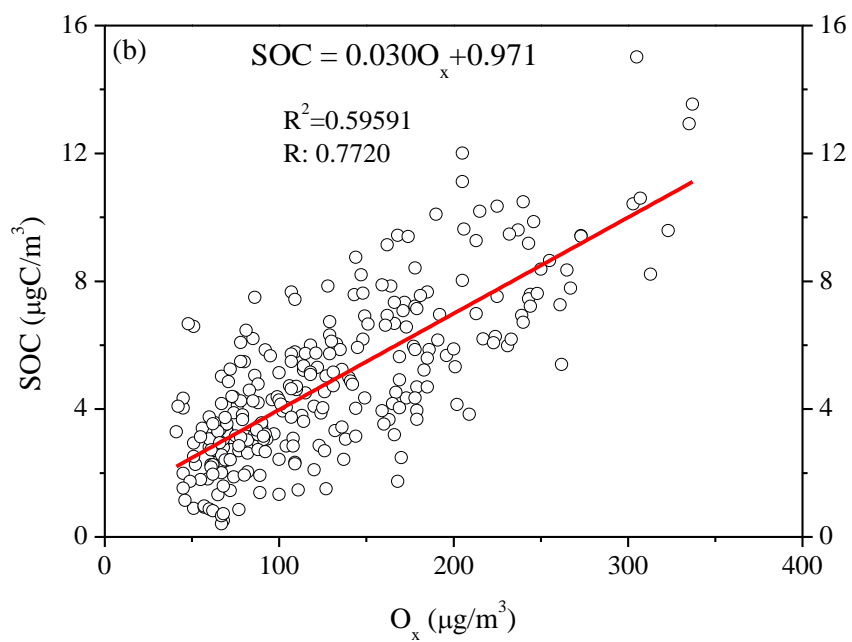
1170

1171

1172

1173

1174



1175

1176

**Figure S5.** Linear correlation between SOC and  $O_x$  concentration.